People's Democratic Republic of Algeria

Ministry of Higher Education and Scientific Research

University Akli Mohand Oulhadj Bouira

Faculty of Sciences and Applied Sciences

Mechanical Engineering Department

A thesis submitted in fulfillment of the requirements for the Master's degree in Mechanical Engineering

Entitled:

Numerical Study on the Impact of Wind Speed on Aerodynamic Parameters in a High-Solidity, Three-Bladed Darrieus VAWT Using 2D k-ω SST Modeling

Presented by: *Belhamdi Hamza*

Before the jury composed of:

		UAMO Bouira	*President*
Aghbari Anis	*Associate Professor, class B*	*UAMO Bouira*	*Advisor*
		UAMO Bouira	*Examiner*
		UAMO Bouira	*Examiner*
		UAMO Bouira	

2023-2024

These pages are lovingly dedicated to my mother, Kheira Rabiai.

To the support that's given me a steady step,

Whenever it gets dark, you're the sunshine,

The melody that takes the silence and turns it into hope,

With every wave of hesitation crashing down in the vast ocean of life,

You were my steady anchor,

Grounding me with that calm companionship,

With that great wisdom, you have steered me through the least difficulty that came across,

Your love gave me the true reason of life,

With each encounter crossed, with each moment of doubt,

You were there, when I had no one on my back,

This work, this journey, is crafted out of your whispers,

In every written word, in every step taken,

Your love formed it all,

For all the sacrifices made in silence,

For all the love that is outside reason,

For you, O heart's eternal home,

As I am, forever and ever, your

Acknowledgments

Praise to Allah, who has guided us to this, and we would never have been guided if Allah had not guided us.

I sincerely thank my supervisor Dr. Aghbari. A for his continuous encouragement and support throughout this research. His valuable insights and expertise played a crucial role in shaping the direction of this work.

I extend my sincere thanks to the members of the jury, for their time and effort in reviewing and judging this work.

As well as I would like to express my heartfelt gratitude to Prof. Mahfoud. B for his valuable advices, his expertise and his constructive feedback were instrumental in overcoming key challenges.

I am profoundly appreciative to all the teachers and personnel of the faculty and university, for support.

Finally, I am also grateful to my colleagues and friends who provided constructive feedback and moral support during this journey. Special thanks to all my family members for their unwavering support and belief in me, which has been my greatest source of motivation.

Abstract:

This thesis investigates the aerodynamic performance of high-solidity Darrieus vertical-axis wind turbines (VAWTs) operating under moderate to high wind conditions using a 2D computational fluid dynamics (CFD) approach. The study employs the SST k-ω turbulence model and solves the unsteady Reynolds-averaged Navier-Stokes (URANS) equations to capture the complex, unsteady flow phenomena around the turbine blades. Key performance metrics such as torque, lift, drag forces, and power coefficient were analyzed across varying tip speed ratios (*TSR*s) and wind speeds to understand their influence on turbine efficiency.

The results revealed that at higher Tip speed ratios and wind speeds, the turbine exhibited improved aerodynamic efficiency due to smoother flow patterns and reduced flow separation. In contrast, lower Tip speed ratios and moderate wind speeds resulted in weaker wake structures and significant flow separation, limiting energy extraction. Critical azimuthal angles for maximum torque and drag forces were identified, emphasizing the importance of blade motion and positioning in optimizing turbine performance. Velocity and pressure contour analyses provided insights into the cyclic aerodynamic forces driving turbine rotation, demonstrating the dynamic interaction between flow patterns and blade geometry.

The findings validate the use of CFD simulations and the SST k-ω model as effective tools for analyzing and optimizing VAWT designs. This work contributes to a deeper understanding of VAWT performance under varying wind conditions and lays a foundation for future research to explore three-dimensional effects, structural dynamics, and additional operational scenarios for further advancing VAWT technology.

Keywords: Aerodynamics of wind turbines, Darrieus, CFD, URANS, SST k-ω.

الملخص:

تهدف هذه المذكرة الى تقديم دراسة التدفق والأداء الديناميكي الهوائي لتربينات الرياح ذات محور الدوران العمودي من نوع داريوس والتي تعمل في ظروف رياح متوسطة إلى عالية باستخدام نهج ديناميكا الموائع الحوسبية (د م ح) الثنائي الابعاد, توظف الدراسة نموذج الاضطراب SST k-ω لحل معادلات رينولدس المتوسطية الغيرمستقرة لنافييه و ستوكس (ر م غ ن س) لالتقاط الظواهر الديناميكية الهوائية المعقدة وغير المستقرة حول شفرات التربينة، لذلك تم تحليل المعايير الرئيسية للأداء مثل العزم، وقوى الرفع والسحب، ومعامل القدرة عبر نسب سرعات دوران وسرعات رياح مختلفة لفهم مدى تأثير هاته المعايير على كفاءة التربينة.

كشفت النتائج ان نسب سرعات الدوران العليا الى جانب سرعات الرياح العليا قد نتج عنها تحسنا في الكفاءة الديناميكية الهوائية بسبب نعومة التدفق وقلة انفصاله عن سطح الشفرات، على عكس نسب سرعات الدوران المنخفضة وسرعات الرياح المتوسطة التي نتج عنها بنيات سحب أضعف وانفصال تدفق معتبرعن سطح الشفرات مما حد من استخراج الطاقة. تم تحديد الزوايا السمتية الحساسة لأقصى عزم وقوى سحب، مما يبرز أهمية حركة الشفرات وتموضعها في تحسين أداء التوربين. كما زودت أنماط كفاف الضغط والسرعة هذه الدراسة ببصائر حول القوى الديناميكية الهوائية الدورية التي تدفع التوربين للدوران، مما يظهر التفاعل الديناميكي بين أنماط التدفق وهندسة الشفرات.

لقد اثبتت النتائج صحة استخدام محاكاة ديناميكا الموائع الحوسبية ونموذجSST k-ω كأدوات فعالة لتحليل تصميمات تربينات الرياح وتحسينها. يساهم هذا العمل في فهم أفضل لأداء تربينات الرياح في ظل ظروف رياح مختلفة ويوفر أساسًا للأبحاث المستقبلية لاستكشاف التأثيرات ثلاثية الأبعاد والديناميكيات الهيكلية والسيناريوهات التشغيلية الأخرى لمواصلة تطوير تكنولوجيا تربينات الرياح.

الكلمات المفتاحية: الديناميكا الهوائية لتربينات الرياح، داريوس، د م ح، ر م غ ن س، SST k-ω.

Résumé :

Cette thèse examine la performance aérodynamique des éoliennes à axe vertical (VAWT) de type Darrieus à haute solidité fonctionnant sous des conditions de vent modéré à élevé, en utilisant une approche de dynamique des fluides numérique (CFD) en 2D. L'étude utilise le modèle de turbulence SST k-ω et résout les équations des Navier-Stokes moyennées en Reynolds non stationnaires (URANS) pour capturer les phénomènes de flux complexes et instables autour des pales de l'éolienne. Les principaux paramètres de performance, tels que le couple, les forces de portance et de traînée, ainsi que le coefficient de puissance, ont été analysés en fonction de différents rapports de vitesse de rotation (*TSR*) et vitesses de vent pour comprendre leur influence sur l'efficacité de l'éolienne.

Les résultats ont révélé qu'à des *TSR* et vitesses de vent plus élevés, l'éolienne présentait une meilleure efficacité aérodynamique en raison de flux plus réguliers et d'une séparation du flux réduite. En revanche, des *TSR* plus faibles et des vitesses de vent modérées ont entraîné des structures de sillage plus faibles et une séparation du flux significative, limitant ainsi l'extraction d'énergie. Des angles azimutaux critiques pour le couple et les forces de traînée maximales ont été identifiés, mettant en évidence l'importance du mouvement et du positionnement des pales pour optimiser la performance de l'éolienne. Les analyses des contours de vitesse et de pression ont fourni des informations sur les forces aérodynamiques cycliques qui entraînent la rotation de l'éolienne, montrant l'interaction dynamique entre les motifs de flux et la géométrie des pales.

Les résultats valident l'utilisation des simulations CFD et du modèle SST k-ω comme des outils efficaces pour analyser et optimiser les conceptions des VAWT. Ce travail contribue à une meilleure compréhension des performances des VAWT sous différentes conditions de vent et constitue une base pour de futures recherches visant à explorer les effets tridimensionnels, la dynamique structurelle et d'autres scénarios opérationnels afin de faire progresser davantage la technologie des VAWT.

Mots-clés : Aérodynamique des éoliennes, Darrieus, CFD, URANS, SST k-ω

Table of contents

List of figures

List of Tables

Nomenclature

λ	Tip Speed Ratio (*TSR*)
ω	Angular Velocity [rad/s]
R	Rotor Radius [m]
U_∞	Free Stream Velocity [m/s]
σ	Solidity
N	Number of Blades
c	Chord [m]
σ_b	Blade's Solidity
AR	Aspect Ratio
H	Blade's Height [m]
D	Turbine Radius [m]
Re	Reynolds Number Based on Blade Velocity
v	Kinematic Viscosity [m^2/s]
W	Blade Relative Velocity [m/s]
V	Blade Absolute Velocity [m/s]
α	Angle of Attack (AoA) [deg]
θ	Azimuthal Angle [deg]
C_L	Coefficient of Lift
C_D	Coefficient of Drag
F_L	Lift Force[N]

F_D	Drag force[N]
F_N	Normal force[N]
F_T	Tangential Force [N]
T	Rotor Toque [Nm]
P	Total Extracted Power [W]
P_{wind}	Available Power in Incoming Wind [W]
ρ	Fluid Density [kg/m^3]
A	Turbine Swept Area [m^2]
$\dot{m}$	Mass Flow Rate [kg/s]
F_{th}	Thrust Force [N]
a	Induction Factor
C_p	Coefficient of Power
C_T	Coefficient of Torque
C_{th}	Coefficient of Thrust
μ_t	Turbulent Dynamic Viscosity [m^2/s]
μ	Dynamic Viscosity [Kg/m.s]
ν_t	Turbulent Kinematic Viscosity [m^2/s]
Δt	Time Step Size [s]
$\Delta \alpha$	Angular Marching Step [Deg]

List of abreviations

VAWT	Vertical Axis Wind Turbine
HAWT	Horizontal Axis Wind Turbine
CFD	Computational Fluid Dynamics
SST	Shear Stress Transport
IEA	International Energy Agency
GHGs	Greenhouse Gases
GWEC	Global Wind Energy Council
WWEA	World Wind Energy Association
NACA	National Advisory Committee for Aeronautics
NASA	National Aeronautics and Space Administration
DES	Detached Eddy Simulation
DNS	Direct Numerical Simulation
BEM	Blade Element Momentum
RANS	Reynolds Averaged Navies-Stocks
URANS	Unsteady Reynolds Averaged Navies-Stocks

Introduction

The global demand for energy is steadily increasing, creating an urgent need for sustainable and environmentally friendly alternatives to traditional energy sources. Renewable energy, particularly wind power, has emerged as a crucial solution to reduce reliance on fossil fuels, limit greenhouse gas emissions, and combat the adverse effects of climate change. Within this sector, vertical-axis wind turbines (VAWTs) are gaining attention due to their distinctive advantages, which make them well-suited for localized power generation in diverse settings, including urban and remote areas.

This thesis investigates high-solidity VAWTs, which are particularly effective in harnessing wind energy in moderate to high wind conditions. Unlike horizontal-axis wind turbines (HAWTs), VAWTs do not rely on complex mechanisms to align with wind direction, making them efficient in environments with variable or turbulent winds. These attributes, combined with their compact design, position VAWTs as a promising choice for both residential and industrial energy applications.

A deeper understanding of the aerodynamic forces influencing turbine blades, the fluid dynamics within the rotor, and the interaction between turbine design and external conditions is essential for improving VAWT's performance. Computational fluid dynamics plays a key role in this analysis, offering a detailed and systematic approach to simulate and evaluate turbine behavior under various operating conditions.

This research focuses on assessing the performance of high-solidity VAWTs under medium to high wind speeds using advanced CFD modeling techniques, specifically the SST k-ω turbulence model. By exploring parameters such as aerodynamic forces, torque, and flow behavior, this thesis contributes to a more nuanced understanding of VAWT functionality and performance optimization.

The findings presented in this work aim to address significant challenges in VAWT design and operation, enhancing their reliability and efficiency while highlighting their potential as a sustainable energy solution for the future.

CHAPTER 1:

Wind power

1.1 Energy production

Over the past few decades, the world's energy consumption has been rising at an exponential rate, mostly as a result of both developed and developing nations' increased energy demands brought on by population growth and rising personal demands. Energy supply has a direct impact on a nation's technological, social, and economic development. This is particularly valid for developing nations. In the modern era, energy has definitely become a basic human need and will remain so for some time to come. The transportation, industrial, commercial/institutional, and residential sectors are the largest energy consumers. Figure 1.1 shows the expansion of the energy supply between 1971 and 2020 as well as the distribution of energy production by source type. According to the International Energy Agency (IEA)[1]. From the same figure, it is evident that fossil fuels like coal, oil, and natural gas continue to provide the majority of the world's energy. Despite their recent growth, energy sources like nuclear, hydro, and renewables still only make up a small portion of the overall supply.

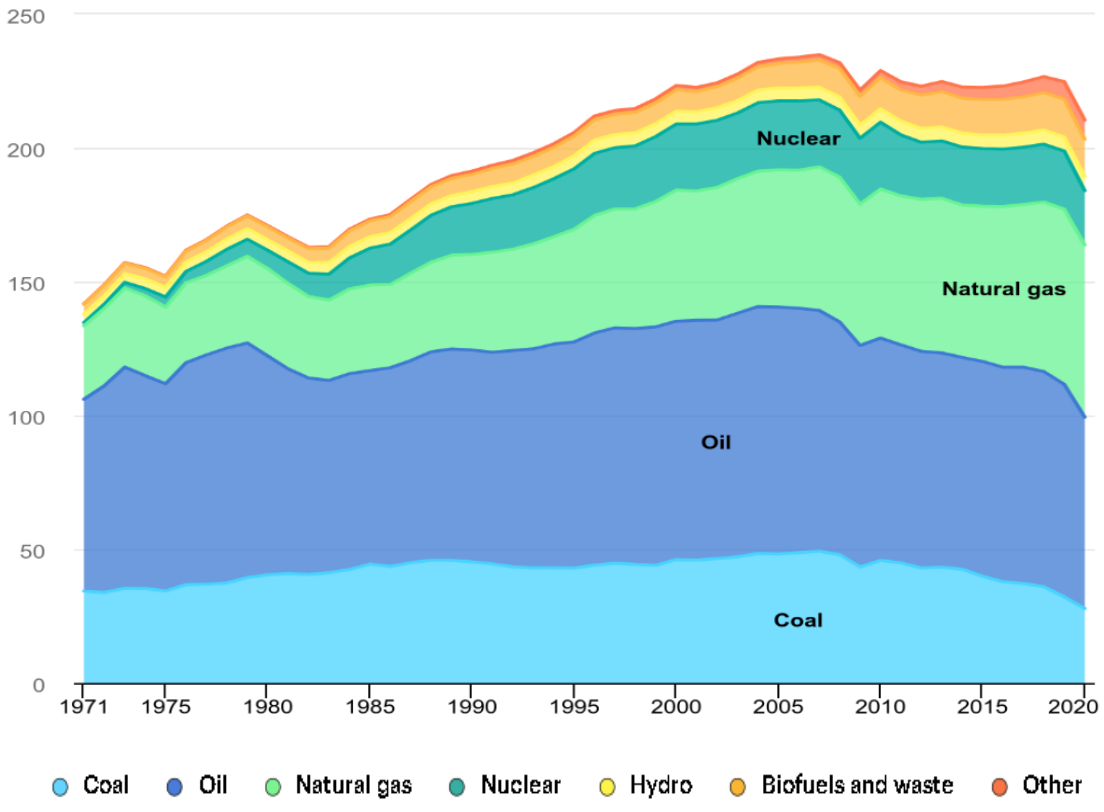

Figure 1.1 OECD Total Energy Supply by Source From 1971 to 2020 [1]

Nearly 97% of Algeria's total energy production comes from fossil fuels, according to F igure 1.2, which was published by the Ministry of Energy and Mines [2]. As it is well known, these energy sources are limited and more significantly, they emit a large amounts of greenhouse gases (GHGs), which in return harm the environment and increase the effects of climate change.

A sustainable and effective renewable energy source is urgently required and meeting this demand has been a goal for many years. Numerous renewable energy sources, including solar, wind, geothermal, hydro, biomass, and tidal, are available for use. Since they lessen dependency on those other limited energy sources and significantly lessen the effects of greenhouse gases, these cleaner and renewable energy sources are receiving more attention in the fight against climate change.

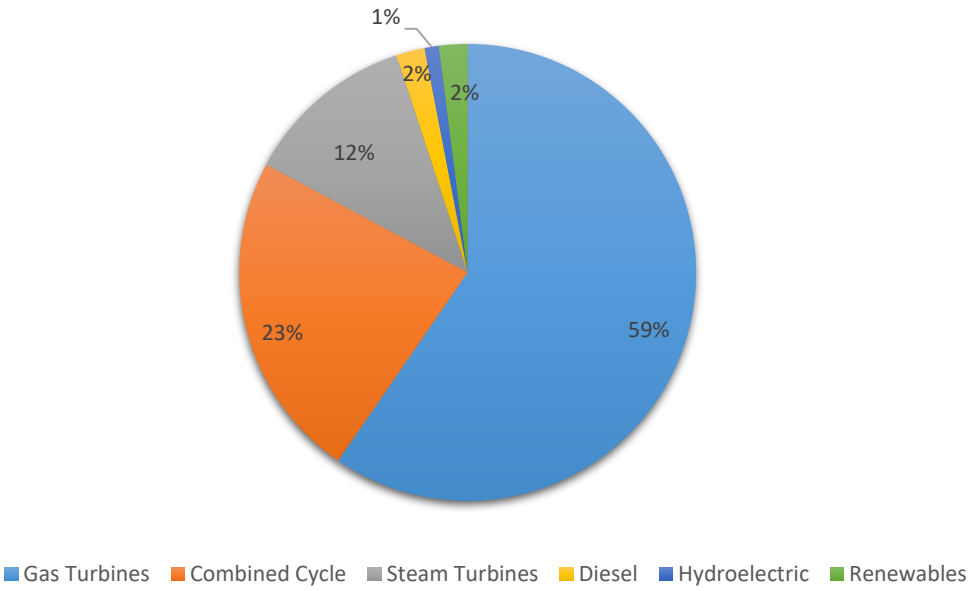

Figure 1.2 Algeria's Installed Power Production Capacity [2]

1.2 Wind energy

The temperature of the atmosphere is distributed unequally due to the curvature of the earth and due to the tilt of its axis which appears in different regions receiving varying amounts of solar energy in form of sun light as shown in Figure 1.3, Warmer air is has a low density and tends to rise, creating areas of low pressure. Cooler air is denser and tends to sink, creating

areas of high pressure The movement of air from high pressure areas to low pressure areas in order to balance the pressure between regions is what we know by wind.

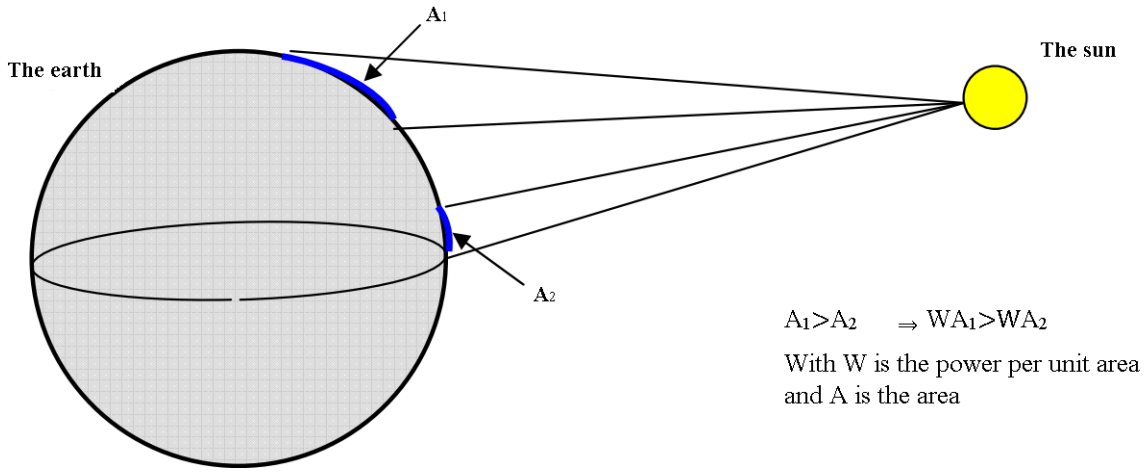

Figure 1.3 Non-Uniform Heating of the Earth's Surface [3]

Historically, wind energy has been utilized to pump water to farms, grind grain, power sailboats, and more recently to produce electricity. One of humanity's oldest energy sources, it has demonstrated enormous promise as a sustainable solution, and its production has increased enormously in recent years. Figure 1.4 demonstrates the ongoing growth of wind energy capacity worldwide, as reported by the Global Wind Energy Council. (GWEC) [4], while Figure 1.5 shows Algeria's potential for wind energy, which is typically quite windy, where about 40% of its surface is characterized by velocities greater than 3 m/s, with 78% of that being greater than 5 m/s [5].

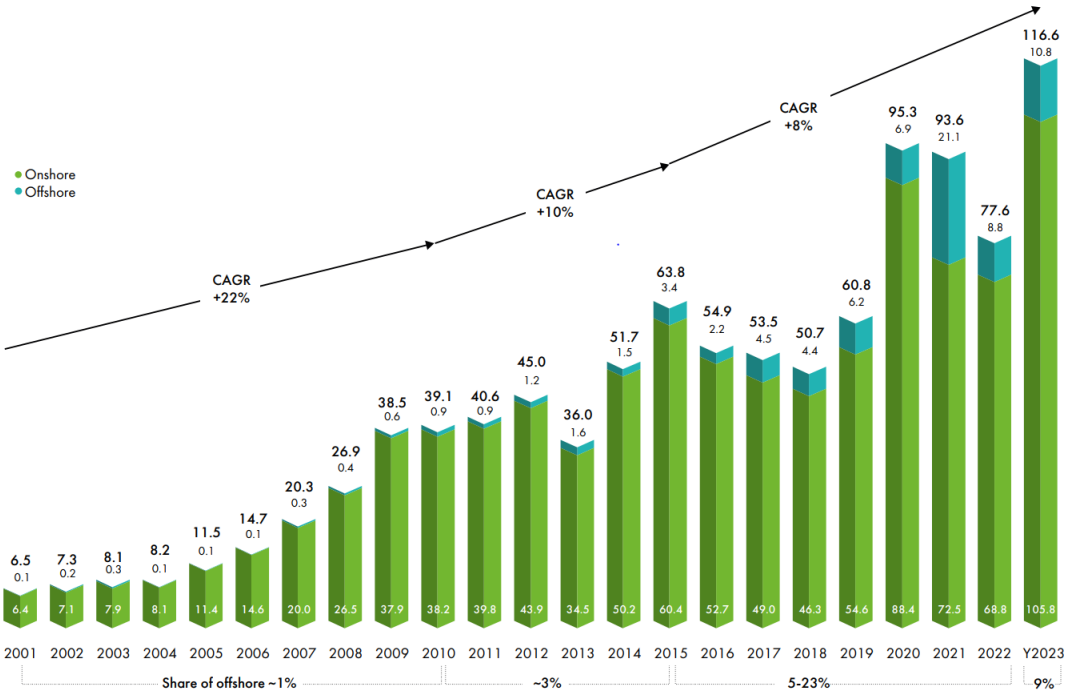

Figure 1.4 Global Installed Renewable Energy Capacity [4]

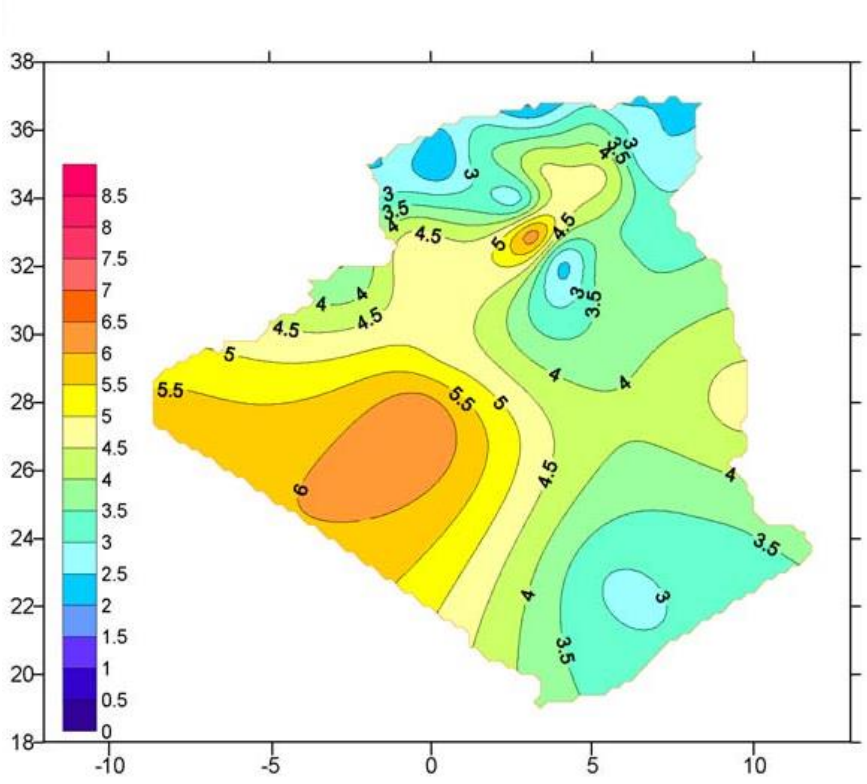

Figure 1.5 Annual Maps of Wind Speed in Algeria at 10 m High [5]

Wind energy has been used both as an alternative for other energy sources and as a supplement to them. Wind turbines come in a wide variety of sizes and uses, which makes them an extremely adaptable energy source. Wind turbines are the most common way of harnessing

wind energy, and they can be harmful to the environment only during their pre-installation phase. For the rest of their life cycles, they emit no GHGs once they are installed. Since their initial use, wind turbines have seen incredible technological advancements, and there is still much room for growth and enhancement. Since their inception, wind turbines have become more efficient and significantly larger due to developments in aerodynamic, structural, and material design.

Both large and small wind turbines have different functions. Large turbines are mostly used in onshore and offshore wind farms; they can usually produce more than 100kW of power. On the other hand, urban settings are where small-scale turbines find their application.

The criterion for accreditation does not exclusively depend on the size of the turbine, but rather on the swept area of the turbine. Historically, large wind turbines have been preferred due to their superior efficiency and substantial power output. However, recent technological advancements have increased the appeal of small-scale wind turbines.

The concept of distributed energy production, where power is generated locally or in close proximity to its consumption point, has made small scale turbines increasingly attractive. This approach offers a cost-effective solution by avoiding issues commonly associated with large scale turbines, such as transportation, transmission cables, and maintenance costs.

The World Wind Energy Association (WWEA) has documented the growth of small wind turbines in terms of capacity and unit numbers in Figure 1.6. This growth underscores the increasing importance and potential of small-scale wind turbines in the energy sector [6].

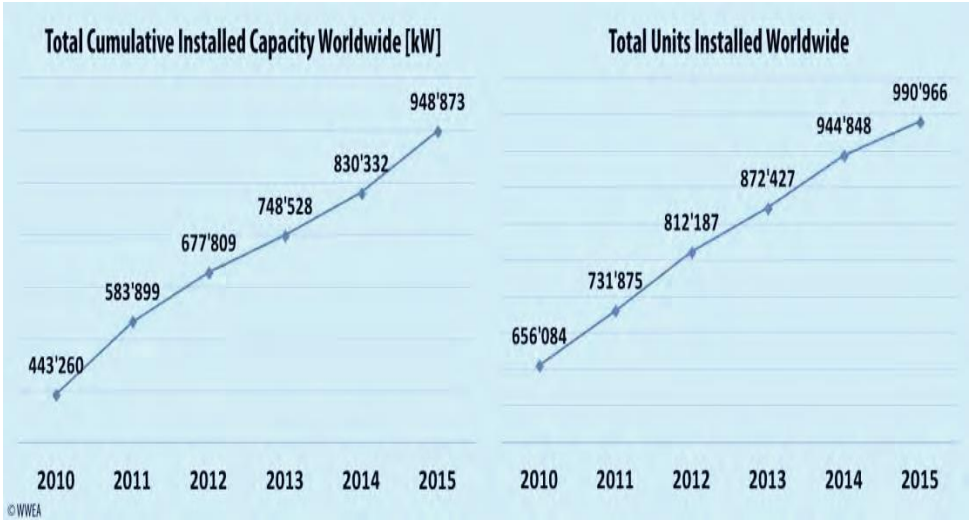

Figure 1.6 Global Installed Energy Capacity and Units [6]

1.3 Wind turbines

1.3.1 A brief history of wind turbines

Regarding the historical origins of wind turbines, there are differing theories. According to some authors, wind energy was first used by humans around 5000 BC, when sailing first appeared. On the other hand, wind turbines have their roots in the stone windmills that the Egyptians built close to Alexandria 3000 years ago [7].

Around 664 BC, in the Persian region of "SEISTAN" (which today borders Afghanistan), the first reliable historical account of windmills that was recorded [8], These mills, which were constructed of cloth and wood, were used to pump water or grind grain. A wind turbine that operates on this principle is depicted in Figure 1.7. It is a vertical-axis wind turbine that is propelled by the wind's force on its blades. Following that, windmill use expanded throughout the Middle East and Central Asia, eventually reaching China and india [9].

Figure 1.7 Vertical-Axis Windmill for Grain Milling, Afghanistan[8]

Early in the Middle Ages, the first 20 windmills were built in Europe. The windmills were originally called "mills" because they were used to pump water and grind grain. They had four blades that rotated on a horizontal axis. The first wind turbine was constructed in 1887 by American scientist Charles F. Brush of Cleveland, Ohio. Figure 1.8 showes that it is 17 meters tall, has 144 cedar blades, and produces 12 kW of power [10]. According to another source, in the same year, Professor James Blyth of Anderson College in Glasgow, Scotland, constructed the first windmill to produce electricity [11].

In 1890, the first "industrial" wind turbine to generate electricity was developed by the Dane Poul La Cour[12]. When it comes to small-scale turbines, the Darrieus wind turbine

concept was created in 1926 by French engineer Georges J.M. Darrieus [13], which has a vertical-axis rotor, not so long after that, an S-shaped concept that is based on the force of drag was invented by the Finnish engineer, Sigurd J. Savonius in 1931 [14].With the growing demand for energy and the technological development of large wind turbines, Denmark's first offshore wind farm with a total capacity of 5 MW was built in 1971.

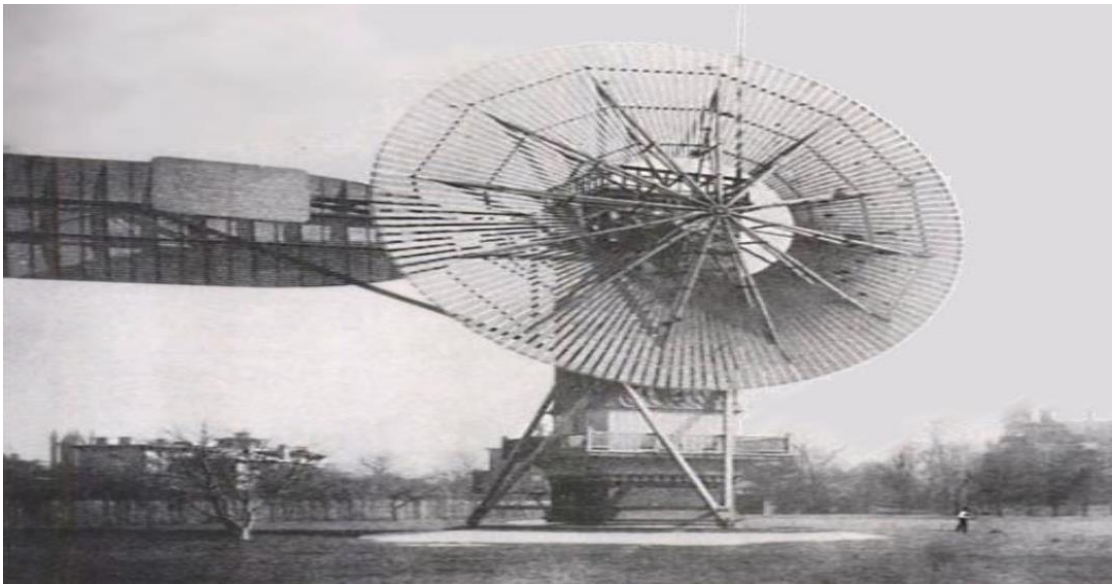

Figure 1.8 Charles Brush's Windmill (1888) [15]

1.3.2 Different types of wind turbines

Wind turbines are classified into two primary groups based on their alignment: horizontal wind turbines (HAWTs) are oriented parallel to the incoming wind, while vertical axis wind turbines (VAWTs) are oriented vertically. VAWTs are a relatively new type of turbines that are developing at a rapid rate, particularly for small and medium-sized turbines that are appropriate for residential or urban locations. There are also growing projects for large VAWTs.

1.3.2.1 Horizontal axis wind turbines

Horizontal-axis wind turbines are based on ancient windmill technology They showed effectiveness, outperforming vertical-axis wind turbines in general, particularly in laminar, high-speed winds. However, they perform poorly in unstable winds or in the case of uncertain direction. HAWTs use aerodynamic profiles and operate based on the force of lift. The number of blades used for this type of turbines typically varies between 1 and 3, with the three-bladed rotor being the most widely used, as it represents a compromise between the rotational speed, cost and the power coefficient. The main characteristics of this type of wind turbine are as follows:

- Max. power coefficient = 45-50%.
- Optimal *TSR* in the range of 5 to 8.
- Starting speed = 4-5m/s

There are two possible configurations as shown in Figure 1.9, each with advantages and drawbacks. The upwind configuration necessitates rigid blades to prevent any possibility of collision with the tower, whereas the downwind configuration permits the use of more flexible rotors. In an upwind machine, the tower's presence barely disturbs the airflow over the blades. While an upwind wind turbine typically requires the use of a specialized device for orientation, a downwind machine can theoretically self-orient based on the direction of the wind. However, the upwind configuration is used by the majority of large wind turbines.

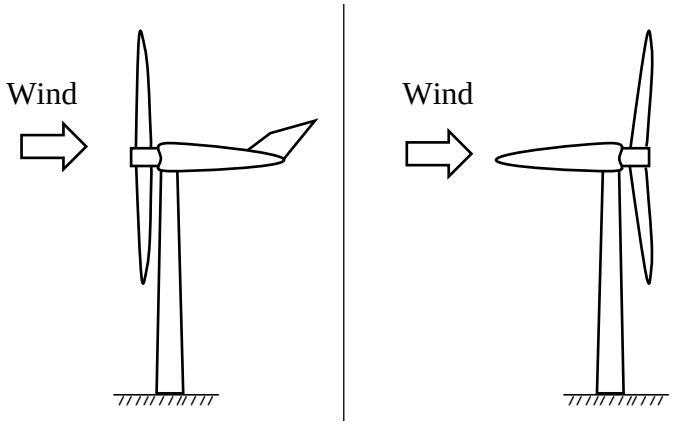

Figure 1.9 HAWTs Rotor Types Depending on Wind Direction

Today, practically the only commercial wind turbines are horizontal-axis. The largest turbines measure up to 280 meters at blade tip, with a rotor diameter of 236 meters and a power output of 15 MW[16] as shown in Figure 1.10.

Figure 1.10 Vestas 33 V236-15.0 MW Large Scale HAWT [17]

1.3.2.2 Vertical axis wind turbines

Vertical-axis wind turbines are more suitable for urban applications, since their operation is independent of wind direction, which is unpredictable in this environment, and they are generally more robust than HAWTs and less noisy. The preferred form for VAWTs, at least for the urban environment, has yet to be clearly identified, as no single model has yet established itself as the best performer. Numerous technological variants have been tested, but only two structures have reached the industrialization stage: the Darrieus rotor and the Savonius rotor.

1.3.2.2.1 Darrieus-type:

Darrieus-type wind turbines have two or three airfoil blades, and operate based on the force of lift. They can be straight-bladed (a), helical (b) or troposkein (c) as illustrated in Figure 1.11. With the generator beneath the turbine, they are more economical than conventional horizontal axis wind turbines. But less efficient. The main characteristics of this type of wind turbines are as follows:

- Max. power coefficient = 20-40%.
- Optimal *TSR* in the range of 1 to 8.
- Starting speed = 4-5m/s

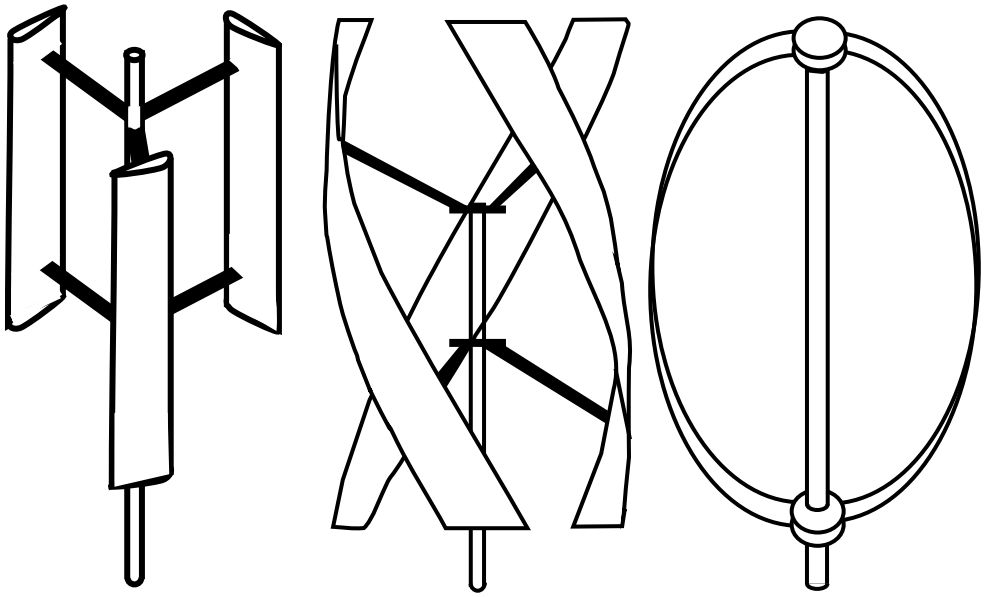

(a) (b) (c)

Figure 1.11 Different Types of Rotors in Darrieus VAWTs

1.3.2.2.2 Savonius-type

Savonius-type wind turbines are made up of two or three blades, generally in the shape of a slightly off-axis half-cylinder (a), three half-cylinders (b) or a twisted blades (c) as shown in Figure 1.12, these turbines operate based on the force of drag. The blade's shape can be straight or twisted. With the generator is located in beneath. The main characteristics of this type of wind turbines are as follows:

- Max. power coefficient = 15-25%.
- Optimal *TSR* in the range of 0.5 to 1.0.
- Starting speed = 2-3m/s

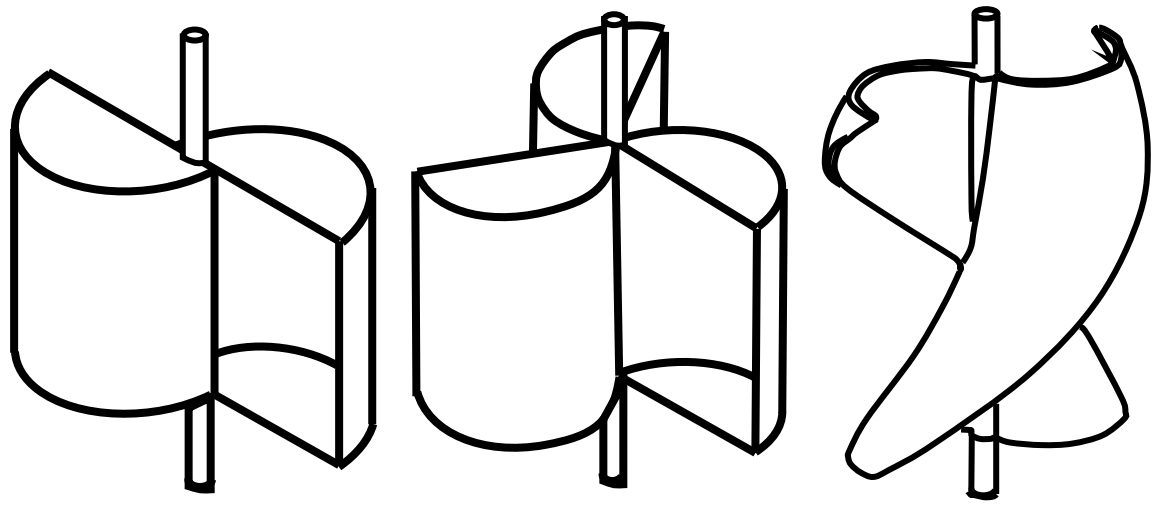

(a) (b) (c)

Figure 1.12 Different Types of Rotors in Savonius VAWTs

The main diffrences between these two types of wind turbines can be summarized in Table 1-1 as follows:

Table 1-1 Summary of the Most Important Differences between H-Darrieus and Savonius Rotors

	H-type Darrieus	***Savonius***
Blade profile	Simple	
Yaw mechanism	No	
Pitch mechanism	Possible	Not possible
Tower	Yes	Optional
noise	Low	
Blade area	Moderate	Large
Guy wires	Optional	
Self-starting	No	Yes
Generator position	On ground	
Foundation	Moderate	
Overall structure	Simple	

1.3.3 Main components of Darrieus VAWT

A Darrieus vertical axis wind turbine generally consists of:

- Tower: Which lifts the main components of the wind turbine from the ground. It is made of metal in order to withstand the weight of the whole system, and it can be bolted to a foundation in the ground, itis defined as the main axis of rotation located at the center of the rotor. The tower allows the generator to be located at the bottom, which facilitates maintenance. since the nacelle is excluded, reducing structural loads.
- Rotor: Which is the most important component of any wind turbine. It sweeps a cylindrical surface as it rotates, so it can harvest the energy of air molecules passing

through, by transforming the wind's kinetic energy into mechanical energy, it consists of:

- Blades: The rotor consists of several straight vertical blades (usually 2 to 3), they have the same shape along their entire length, with an aerodynamic profile or a bucket shape that enables them to absorb wind energy and rotate to turn main shaft, thus generating mechanical rotational energy. are subject to high bending moments, due to the centripetal acceleration this effect diminishes with increasing turbine size increases.

  Blade design is much simpler in this type of wind turbines, they can be made of composite materials such as carbon fibers or fiber glass and resin or aluminum alloy, making them lightweight, ensuring sufficient rigidity and strength.

- Radial arms: It is the central horizontal component that connects the blades and the drive shaft is typically a structural element designed to provide support, stability, and rotational movement to the blades as they interact with the wind, it consists of a central shaft or spindle around which the turbine blades are mounted. The blades are evenly spaced and attached to the hub at regular intervals along its circumference, as it may include additional features such as bearings, seals, and mounting hardware to facilitate smooth rotation and efficient operation of the turbine.

- Generator: It is where the wind's kinetic energy is transformed into electrical energy, the generator's design and manufacturing is based on efficiency, cost and minimum maintenance requirement, since size is not the main concern, as it is installed at the bottom of the tower. The generator often has a direct drive system, meaning that the turbine is connected directly to the generator rotor via a shaft, which guarantees more efficiency than a gearbox generator, makes it simpler, easier to install and less expensive.

1.3.4 Working principle of VAWTs

The conversion of wind power occurs in two distinct phases:

- In the first phase rotor captures a portion of the wind’s kinetic energy and converts it into mechanical work. This phenomenon is made possible by the use of an aerodynamic profiles in the case of Darrieus turbine, or a bucket-shaped blades in the case of Savonius

turbine placed in an air flow at various angles, which is then subjected to forces of different intensities and directions as illustrated in Figure 1.13.

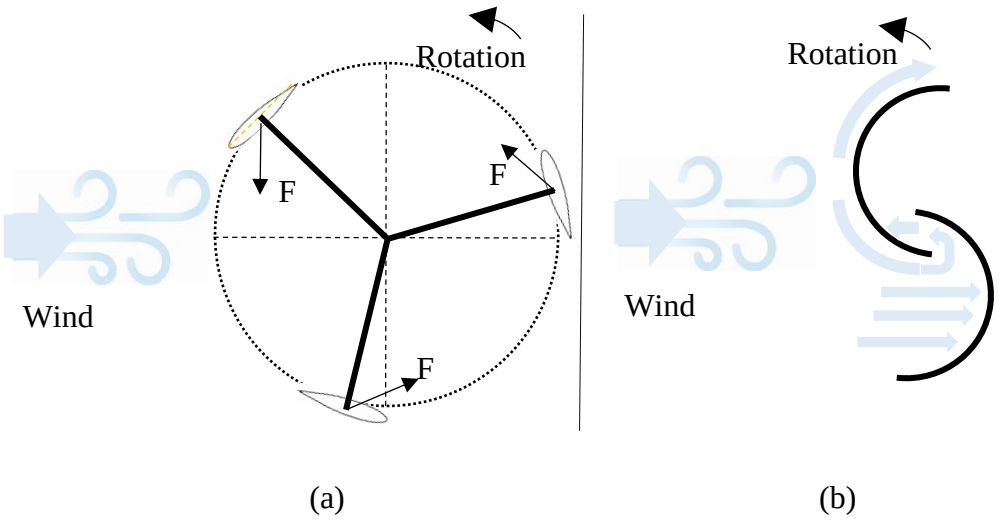

Figure 1.13 Working Principle of Conventional VAWTs' Rotors

This illustrates the fundamental principle of fluid mechanics, where the interaction between a blade and an air flow generates variable forces, thus allowing the conversion of the wind's kinetic energy into mechanical energy. When these forces combine, a driving torque is produced.

- at the ground level, where the generator is situated. Because the turbine is directly connected to the generator rotor via a shaft, it is coupled to an electrical generator that produces either direct current or alternating current. As a result, it transforms mechanical energy into electrical energy, which is subsequently sent to electrical grids. Moreover, the vertical wind turbine doesn't require any orientation device because it runs in any direction the wind blows.

1.4 Motivation

In urban areas and spaces with frequent shifts in wind direction, VAWTs suitable and practical to deploy, as they can capture wind from any angle, unlike traditional HAWTs that may involve yaw mechanism, which can add more cost and complexity. These turbines also have a unique advantage in regions where wind speeds are typically low to moderate, enabling wind power to be harnessed in places where it hasn't been practical before. By exploring their

performance in both moderate and high winds, this study aims to analyze H-Darrieus design particularly in both medium to high winds in order to examin the performance trends and how would the turbine behavior be under the mentioned conditions. Additionally, this research supports the shift toward distributed, small-scale energy systems, which can provide reliable power in urban areas, remote locations, and regions where large-scale energy infrastructure is limited. Ultimately, understanding how VAWTs operate not only advances wind technology but also aligns with global efforts to transition to clean, accessible, and resilient energy sources. This study aims to help make wind energy a practical, sustainable choice for a wider range of communities and environments.

1.5 Applications of VAWTs

The Vertical Axis Wind Turbine has been successfully implemented in a variety of applications, from power generation to lighting systems. The following points provide a brief overview of these applications:

- Power generation: Wind turbines, particularly VAWTs, are widely recognized and utilized for power generation globally. They are commercially available for electricity production.
- Energy recovery systems: Numerous research initiatives around the world are exploring the use of VAWTs in systems designed for energy recovery.
- Water pumping: VAWTs have been employed in mechanical applications for water pumping where it is hard and expensive to use electricity from the power grid directly.
- Telecommunications/Grid monitoring: VAWTs are increasingly being adopted in the telecommunications sector. They are used for monitoring mobile stations in countries such as Korea, China, among others.
- Wind & Solar lamps: Wind-solar hybrid systems for applications like parking lots are being developed in various countries, such as Japan. These systems predominantly rely on VAWTs.
- Polar research station systems: VAWTs have been utilized in Antarctica for power supply generation.

1.6 Conclusion

To conclude, this chapter has presented an overview of wind power and the essential principles behind wind turbine operation. Wind energy, as a renewable resource, is vital for sustainable electricity generation, with turbines converting the kinetic energy of wind into mechanical power. Key aspects of turbine function, such as the roles of lift and drag forces in rotor movement, have been discussed. As the world transitions toward cleaner energy sources, a solid understanding of these foundational concepts is crucial for improving turbine design and optimizing energy production. The following chapters will explore the technical details and practical applications of wind turbine systems in greater depth.

CHAPTER 2:

Aerodynamic considerations

2.1 Parametres and refrence systems

2.1.1 Wind speed and Tip Speed Ratio

Wind speed is a critical factor influencing the efficiency and overall performance of wind turbines. The interaction between the velocity of the wind and the motion of the turbine blades is represented by the tip speed ratio (*TSR*), a dimensionless quantity that describes the ratio of the blade tip's velocity to the wind speed. This parameter is essential for understanding the turbine's aerodynamic characteristics and optimizing its operation. The *TSR* is defined as:

$$\lambda = TSR = \frac{\omega R}{U_\infty} \quad (1)$$

In this context, ω represents the angular velocity, R is the turbine radius, and U_∞ denotes the velocity of the free stream. The selection of a λ also depends on the generator available to convert the mechanical energy of the spinning wind turbine into electricity. Some generators are not able to operate at low values of ω.

2.1.2 Geometry definition

The solidity is a dimensionless parameter referring to the ratio of the total area swept by the rotor blades to the area of the rotor's circular cross-section can be used to define the geometry of the VAWT.

$$\sigma = \frac{Nc}{2R} \quad (2)$$

It essentially quantifies how densely the rotor blades occupy the space through which the wind flows, where n is the number of blades, c is the chord length.

Solidity is an important parameter in VAWT design as it directly influences the aerodynamic performance and efficiency of the turbine. A higher solidity generally leads to greater torque production, but it can also increase drag and reduce efficiency if the blades are too closely spaced [18]. By adjusting the number of blades and their size relative to the rotor diameter, the solidity can be optimized to achieve the desired balance between torque production, efficiency, and structural considerations.

Blade's solidity $\sigma_b$may also be defined, which is equal to the ratio between the blade chord and the rotor radius

$$\sigma_b = \frac{c}{R} \quad (3)$$

Another parameter is Aspect Ratio, which is defined as the ratio between height and radius of the rotor.

$$AR = \frac{H}{D} \quad (4)$$

The Reynolds number is used to characterize the flow regime confronted by the blades. It signifies the ratio between inertial forces and viscous forces. For the current study of a Darrieus machine blade, a characteristic Reynolds number is generally chosen from the rotational speed, so that there is no dependence on blade position. Its expression is as follows:

$$Re = \frac{R\omega c}{v} = \frac{\lambda U_\infty c}{v} \quad (5)$$

2.1.3 Reference systems and orientations

Since the Darrieus wind turbine has blades that rotate around an axis, changing the reference frame is an easy-to-use tool for studying different aspects of the machine. Figure34 lists all the reference frames used. They are defined in three dimensions, but for most of our studies, we'll be working in a transverse plane.

To define the machine's global characteristics and performance it is necessary to define a global reference frame (O; $\overrightarrow{e_x}$; $\overrightarrow{e_y}$; $\overrightarrow{e_z}$). This is a fixed Cartesian coordinate system. The point O is fixed at the axis of rotation, the director vector $\overrightarrow{e_x}$ is oriented in the direction of the flow, the vector $\overrightarrow{e_y}$ points to the position where the blade is placed when it is oriented facing the infinite upwind.

To understand how the driving force is generated at the blade, a rotating reference point is defined ($P_{att}; \overrightarrow{e_n}; \overrightarrow{e_t}; \overrightarrow{e_z}$) linked to the blade. Where P_{att} is the attachment point of the blade, $\overrightarrow{e_n}$ is the director vector normal to the profile oriented towards the outside of the rotor, and $\overrightarrow{e_t}$ is tangent to the profile, oriented towards the leading edge. Thus, a force will be driving if its component along $\overrightarrow{e_t}$ is positive. In addition, this basis can be used to define an azimuthal position of the blades, noted θ, which is the angle formed between the vectors $\overrightarrow{e_y}$ and $\overrightarrow{e_n}$. This choice makes it possible to distinguish between an upstream phase of rotation ($0° \leq \theta < 180°$) and a downstream phase of rotation ($180° \leq \theta < 360°$). Two remarkable zones can be distinguished as well, that sometimes mentioned: upwind (θ = 0°) and downwind (θ =180°) profile zone. By convention, in the presence of several blades, the azimuthal position of the rotor is limited to the azimuthal position of a reference blade initially located facing the wind.

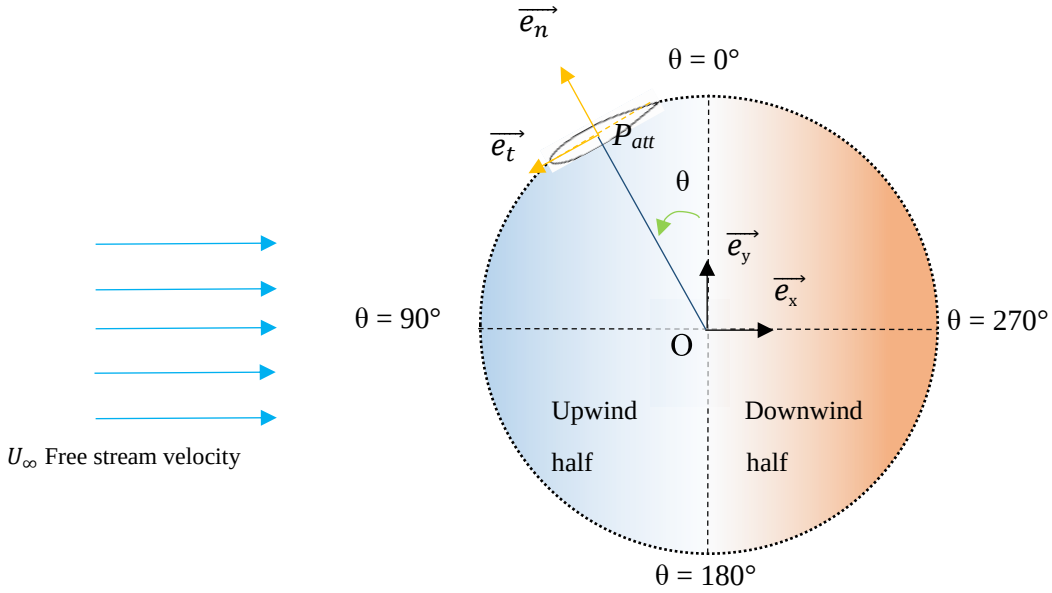

Figure 2.1 Definition of Reference Frames and Associated Bases in a Cross-Sectional View

When pressure distributions or boundary layer properties need to be defined, it is sometimes more useful to define a base $(\overrightarrow{e_\tau}; \overrightarrow{e_v}; \overrightarrow{e_z})$ linked to the surface of the airfoil. The vector $\overrightarrow{e_\tau}$ is tangent to the surface of the foil, $\overrightarrow{e_v}$ is normal to the profile oriented towards the outside of the profile. This is particularly useful when curvilinear coordinates are involved. To measure the curvilinear abscissa along the profile surface, the choice is made to rotate clockwise, starting from the trailing edge so the inner face of the profile (facing the axis of rotation) is crossed before the outer face.

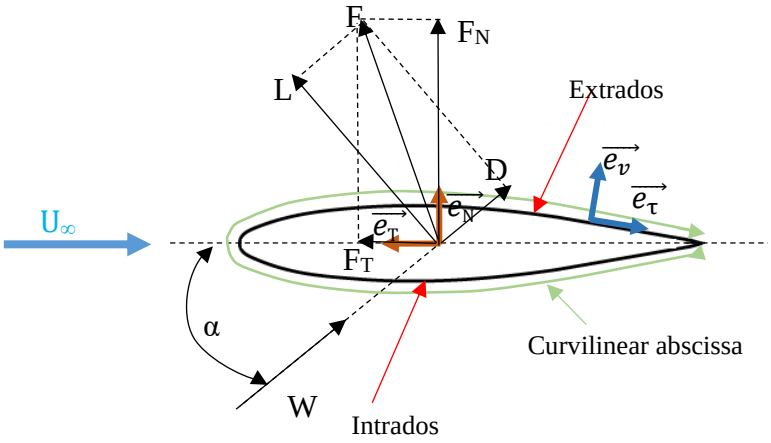

Figure 2.2 Definition of Reference Frames and Main Orientations (Angle of Attack, Curvilinear Abscissa and Applied forces on the Airfoil) in a Cross-Sectional View

In the event that the forces applied on the intrados and the extrados for a translational profile are well defined on the positive-lift side According to Bernoulli's principle as the speed of the airflow increases, the pressure decreases. The air accelerates over the curved upper surface, resulting in a lower pressure-region above the airfoil.

In contrast. the flow under the airfoil is generally slower and the pressure is relatively higher compared to the upper surface. This pressure difference between the upper and lower surfaces contributes to the generation of lift.), then the surfaces for a Darrieus blade profile alternate between being under suction (negative pressure) and under pressure (positive pressure), with the inner face facing the rotational axis. Likewise, the angle of attack (*AoA*) is considered positive when the incident flow strikes the lower face (intrados) first. order to keep the notation similar when the blade is in its initial azimuthal position (θ = 0°), the *AoA* is then positive for the downwind phase and negative for the upwind phase.

2.2 Performance prediction

For ease of understanding, a simplified operating principle is described here where the aerodynamic torque is negligible, it means that the attachment point is the point where the aerodynamic forces are applied. The radius of the machine and the angular velocity are assumed to be constant. The blade rotating around the axis of rotation is confronted with a relative speed, or the speed from the blades point of view, noted $\vec{W}$. The latter notation indicates that this is the speed in the blade's frame of reference. It results from the change of reference frame, which is expressed as the vector combination of the infinite upstream speed and the rotational speed if disturbances are neglected:

$$\overrightarrow{W} = \overrightarrow{U_\infty} - \overrightarrow{\omega}\left(\vec{X} - \overrightarrow{X_0}\right) = \overrightarrow{U_\infty} - \overrightarrow{V} \quad (6)$$

Where :

$$\overrightarrow{V} = \overrightarrow{\omega} \times \left(\vec{X} - \overrightarrow{X_0}\right) \quad (7)$$

$\overrightarrow{V}$ Is the speed induced by blades rotation at the attachment point, for $\vec{X}$ =$\overrightarrow{X_{att}}$, $\overrightarrow{V}$=$R\omega\overrightarrow{e_t}$. The *AoA* at the attachment point can be deduced from the projection of the relative velocity in the two-dimensional reference frame linked to the profile ($\overrightarrow{e_n}$; $\overrightarrow{e_t}$):

$$\alpha = arctan\left(\frac{\overrightarrow{W}}{\overrightarrow{W}}\frac{\overrightarrow{e_n}}{\overrightarrow{e_t}}\right) \quad (8)$$

Expressing the relative speed as a function of the dimensionless operating parameters, the relation is expressed as:

$$\alpha = -arctan\frac{sin\,(\theta)}{\lambda + cos\,(\theta)} \quad (9)$$

The *AoA* alternates between a negative and positive sign in the upstream phase and the downstream phase respectively. Similarly, relative velocity evolves with azimuth angle according to the following relation:

$$\|\vec{w}\| = U_r = U_\infty\sqrt{1 + 2\lambda\,cos(\theta) + \lambda^2} \quad (10)$$

The presence of a non-zero incidence on the blades profile generates a force F on the profile (Figure 2.4), which can be broken down into drag force F_D (in the direction of relative speed) and lift force F_L (perpendicular to relative speed). The forces of lift and drag are related to their respective dimensionless coefficients C_L and C_D, the coefficients themselves being deducible from incidence and relative speed. If we project the force F onto the reference frame linked to the profile, we obtain the tangential force F_T and the normal force F_N. The normal force expressed at the point of attachment is systematically in the axis of a radius and does not contribute to blade rotation. The tangential force represents the driving (or resistive) component

of the aerodynamic force. F_T and F_N can be written as a function of lift and drag using geometrical Equations involving incidence.

The instantaneous torque T that the force delivered to the rotor is expressed as the product of the tangential force and the rotor radius. The average torque $\overline{T}$ can be deduced by averaging the instantaneous torque over one rotation. Then, its product by angular speed gives the average power $\bar{P}$ generated by aerodynamic forces. For N blades, the average power is expressed by:

$$\bar{P} = \sum_{n=1}^{N} \frac{\omega}{2\pi} \int_0^{2\pi} T(\theta) d\theta = \frac{NHR\omega}{2\pi} \int_0^{2\pi} F_t(\theta) d\theta \qquad (11)$$

When an air flow passes through a wind turbine, it can absorb the energy of the mass flow and convert it into rotational energy. However, this energy cannot be fully recovered. The aerodynamic power coefficient (Equation (12)) is therefore defined as the ratio between the average power and the kinetic power of the wind passing through the surface swept by the machine. Similarly, torque coefficient C_T can be determined, a dimensionless version of the torque given by Equation (13):

$$C_P = \frac{\bar{P}}{\frac{1}{2}\rho A U_\infty^3} = \frac{\overline{T}\omega}{\frac{1}{2}\rho A U_\infty^3} \qquad (12)$$

$$C_T = \frac{\overline{T}}{\frac{1}{2}\rho R A U_\infty^3} = \frac{C_p}{\lambda} \qquad (13)$$

As a result, the power coefficient can be formulated as:

$$C_P = \frac{\overline{T}\omega}{\frac{1}{2}\rho A U_\infty^3} \qquad (14)$$

With Wind power, which is the maximum kinetic energy available in the wind as it passes through the rotor area, is expressed as follows:

$$P_{wind} = \frac{1}{2}\dot{m} U_\infty^2 \qquad (15)$$

$\dot{m}$ represent the air mass flow rate passing through each rotor, they are expressed by:

$$\dot{m} = \rho U_{\infty} A \tag{16}$$

Where ρ is the density of the air, and A is the cross-sectional area of the rotor as shown in Figure 2.3, they are expressed by:

$$A = D \times H \tag{17}$$

With:

- D: Rotor's diameter,
- H: Rotor's height,

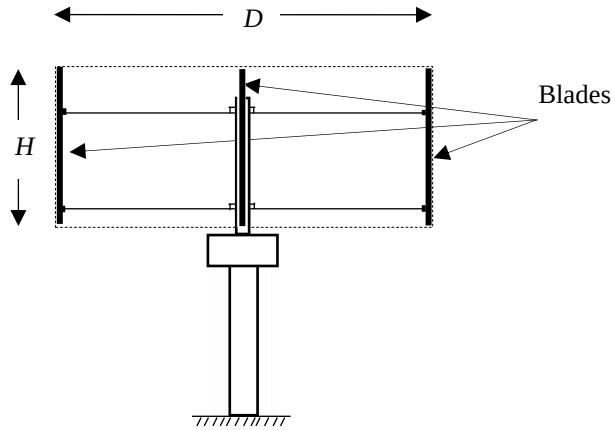

Figure 2.3 Schematic Side-View of the Turbine's Cross-Section

Hence this power can be expressed by:

$$P_{wind} = \frac{1}{2}\rho A U_{\infty}^{3} \tag{18}$$

The turbine's driving force is generally provided by lift, and its resistive counterpart is mainly due to drag. The tangential force can be expressed from the lift and drag coefficients:

$$F_T = \frac{1}{2}\rho c U_r^3 [C_L \sin(\alpha) - C_D \cos(\alpha)) \tag{19}$$

Over the range of encountered incidence angles, in general, the $C_L \sin(\alpha)$ term predominates over the $-C_D \cos(\alpha)$, except for areas where incidence is too low, in other words. For azimuths of θ=0° and θ=180°. therefore, two driving zones upstream and downstream of the rotation are defined, as well as two resistive zones in the upwind and downwind blade zones (figure 2.4).

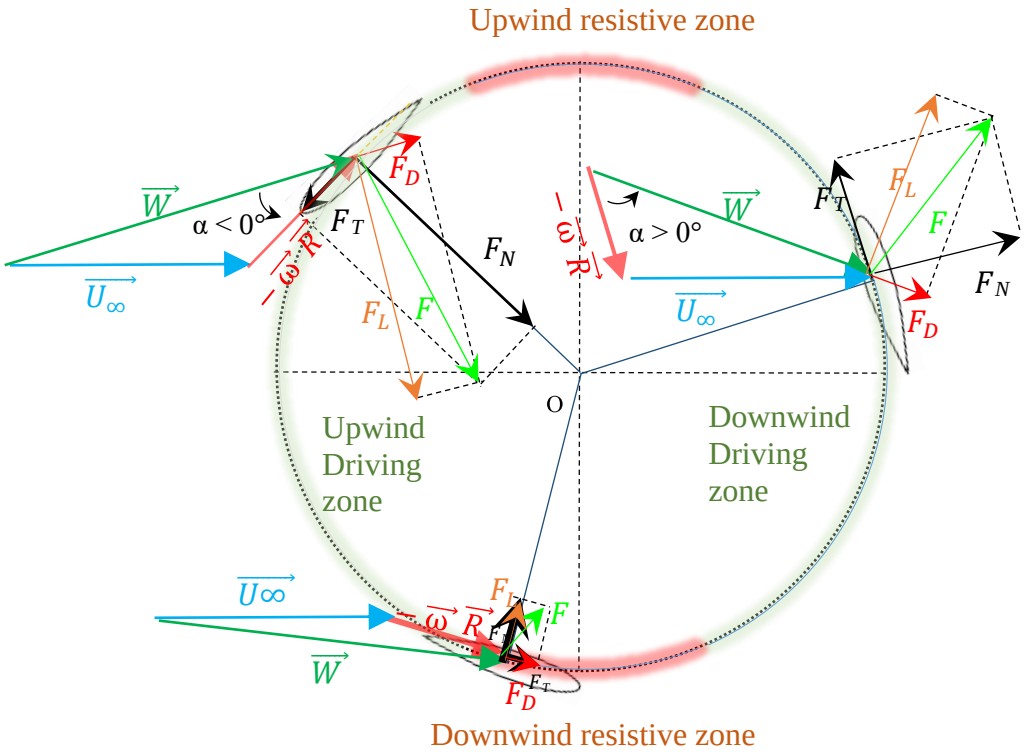

Figure 2.4 Representation of: Applied forces, Classical Velocity Triangle, Resulting lift and Drag Forces, Projection of the Total Force Along the Normal and Tangential Directions to the blade's Chord, Upwind and Downwind Driving Regions and Resistive Regions

By combining Equations (11), (12) and (19) and considering *N* identical blades, we can directly express the power coefficient as a function of the lift and drag coefficients:

$$C_p = \frac{\sigma\lambda}{2\pi}\int_0^{2\pi}\left(\frac{W}{U_\infty}\right)^2 [C_L \sin(\alpha) - C_D \cos(\alpha)]d\theta \qquad (20)$$

Equation (20) reveals that for a given rotor geometry, the power coefficient is mainly a function of *TSR*, relative speed and *AoA* (the aerodynamic coefficients being a function of the latter two parameters). However, relative flow velocity and incidence are themselves attributes that depend on *TSR* through Equations (9) and (10), making *TSR* the fundamental parameter that modulates machine's efficiency.

2.2.1 Ideal performance and the Betz Limit

The purpose of wind turbines is to effectively capture wind energy, early calculations by Albert Betz suggested a theoretical maximum efficiency of 59.3%. This limit was calculated under perfect wind turbine circumstances, which included no rotational velocity in the wake and frictionless operation [19]. Nevertheless, friction and vorticity shedding occur in real-world turbines, requiring more precise prediction techniques. Analyzing the flow along a streamtube that passes through the rotor is essential to comprehending the distribution of wind load on the rotor. The rotor surface is assumed to have uniform pressure over it, and pressure loss occurs as air passes through it. This method is referred to as one-dimensional momentum theory.

In ideal rotor and wind conditions, where there are no mechanical or aerodynamic losses, the air is stationary, incompressible, and frictionless, no outside forces are acting on it, and the static pressure equals the ambient pressure away from the rotor, these principles hold true, according to Betz [20].

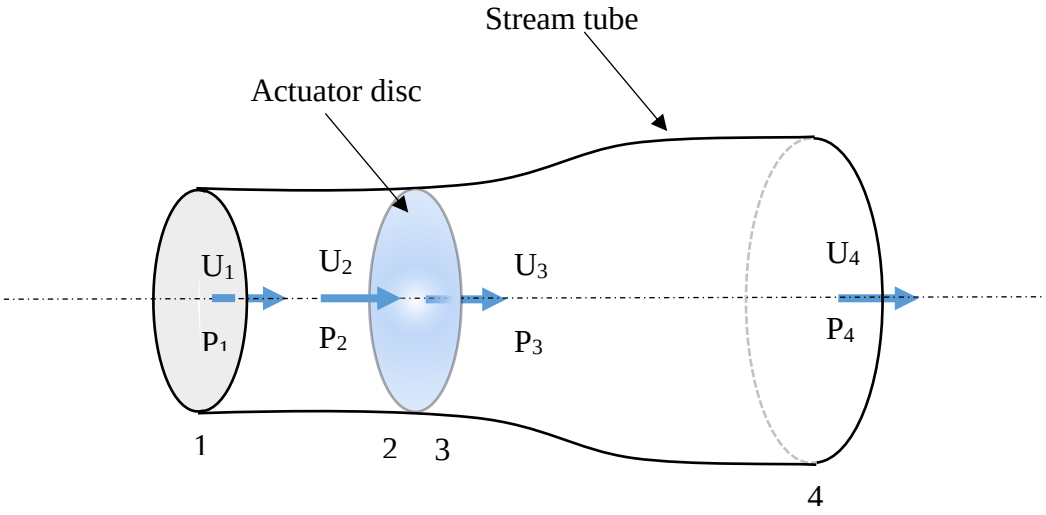

Figure 2.5 Diagram Illustrating the Parameters Used to Determine the Betz Limit

Considering the system shown in Figure 2.5, with wind speed U_2 upstream (position 2) and wind speed U_3 downstream (position 3).

The loss of air pressure across the rotor results in a thrust force F_{th} applied by the air to the rotor. The conservation of linear momentum in the control volume allows us to express this force as follows:

$$F_{th} = U_1(\rho AU)_1 - U_4(\rho AU)_4 \qquad (21)$$

Where A_1 and A_4 are the upstream (position 1) and downstream (position 4) sections respectively. By applying the principle of mass conservation in the control volume:

$$\dot{m}_1 = \dot{m}_4 = \dot{m} \leftrightarrow (\rho A U)_1 = (\rho A U)_1 \quad (22)$$

By replacing the equation 21 into the equation 20:

$$F_{th} = \dot{m}\,(U_1 - U_4) \quad (23)$$

By applying the Bernoulli's principle between sections 1 and 2 upstream of the rotor and between sections 3 and 4 downstream of the rotor.

$$p_1 + \frac{1}{2}\rho U_1^2 = p_2 + \frac{1}{2}\rho U_2^2 \quad (24)$$

$$p_3 + \frac{1}{2}\rho U_3^2 = p_4 + \frac{1}{2}\rho U_4^2 \quad (25)$$

Since the pressure upstream (position 1) and downstream (position 4) is the same due to continuity, and the wind speed in the section just before and after the rotor is assumed to be equal.

$$p_1 = p_4 \quad (26)$$

$$U_2 = U_3 \quad (27)$$

Finally, it is found that:

$$F_{th} = A\,(p_2 - p_3) \quad (28)$$

The thrust force is thus the cross-sectional area of the rotor multiplied by the pressure difference upstream and downstream of the rotor. This force can also be written as a function

of density ρ and wind speed U_1 and U_4, by replacing equations (24) and (25) into equation (28) to obtain:

$$F_{th} = \frac{1}{2}\rho A(U_1^2 - U_4^2) \quad (29)$$

By equalizing (29) and (23) it gives:

$$U_2 = \frac{U_1 + U_4}{2} \quad (30)$$

Again, based on the principle of conservation of mass, the appearance of excess pressure upstream of the rotor leads to a reduction in the incident wind speed. The axial induction factor "a" as the proportion of speed reduction between the incident wind and the wind passing through the rotor. It is defined as follows:

$$a = \frac{U_1 + U_2}{U_1} \quad (31)$$

The wind speed at position 2 is then expressed as a function of the wind speed at position 1, upstream of the rotor, by:

$$U_2 = U_1(1 - a) \quad (32)$$

And the wind speed at position 4 is expressed as a function of the axial induction factor by:

$$U_4 = U_1(1 - 2a) \quad (33)$$

The power generated by this pressure drop when the wind passes through the rotor is given by:

$$P = F_{th} U_2 \quad (34)$$

Given $A_1 = A$ the cross-sectional area of the rotor, and the wind speed $U_1 = U$ and by combining equations (29), (32) and (33) allows to express the thrust as:

$$F_{th} = \frac{1}{2}\rho A U^2 (4a)(1 - a) \tag{35}$$

Power can be expressed using equations (29), (32) and (33) as follows:

$$P = \frac{1}{2}\rho A U^3 (4a)(1 - a)^2 \tag{36}$$

Based on these definitions, it is possible to derive dimensionless expressions for power and thrust, which define the power coefficient C_p and the thrust coefficient C_{th}.

$$C_p = \frac{P}{\frac{1}{2}\rho A U^3} = 4a(1 - a)^2 \tag{37}$$

$$C_{th} = \frac{T}{\frac{1}{2}\rho A U^2} = 4a(1 - a) \tag{38}$$

The Betz limit can be determined by differentiating the power coefficient expression with respect to the axial induction factor to obtain the value of this factor that maximizes the power coefficient.

$$\frac{dC_p}{da} = 0 \quad \rightarrow \quad C_{p,max} = C_{p(a\,=\,1/3)} = \frac{16}{27} = 59{,}26\% \tag{39}$$

This maximum value of C_p is called the Betz limit. It is a theoretical maximum, meaning that it is not possible to extract more than 59.3 % of the energy from an airflow. This value is achieved for $a = \frac{1}{3}$.

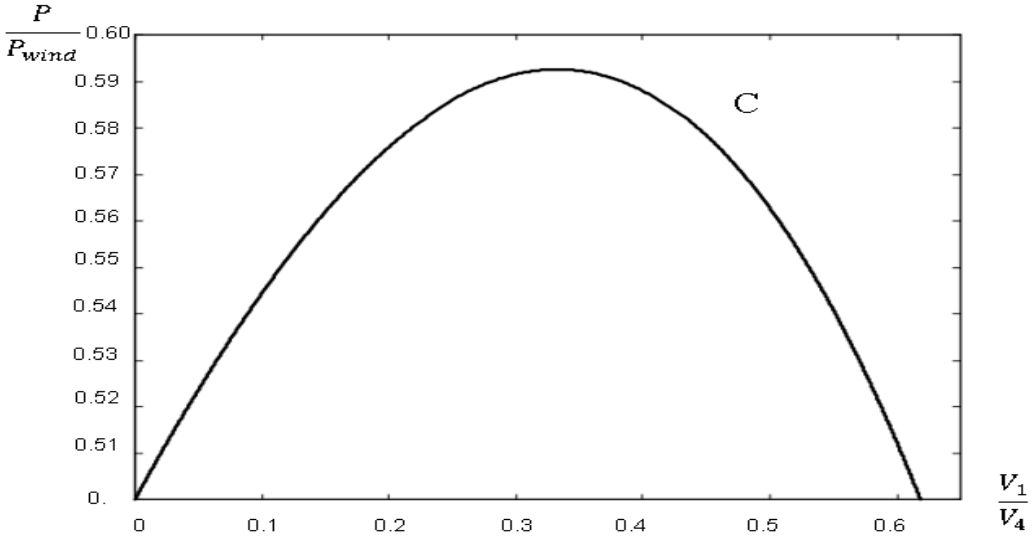

Figure 2.6 Power Coefficient Curve [21]

The curve shown in figure 2.6 represents the most common shape of the power coefficient of an ideal wind turbine. This shape can change depending on the type of turbine (vertical or horizontal) or the number of blades, as shown in figure 2.7.

This figure shows the typical power curves for the most common types of turbines, where it can be seen that HAWTs are typically more aerodynamically efficient and operate at much higher *TSR* values than VAWTs, the $C_p = f(\lambda)$ curve has a rather narrow, pointed bell shape for slow wind turbines with a *TSR* varying from 0 to 6. Whereas for fast wind turbines with a *TSR* above 6, the shape of this curve is rather wide and flattened at the top.[21]

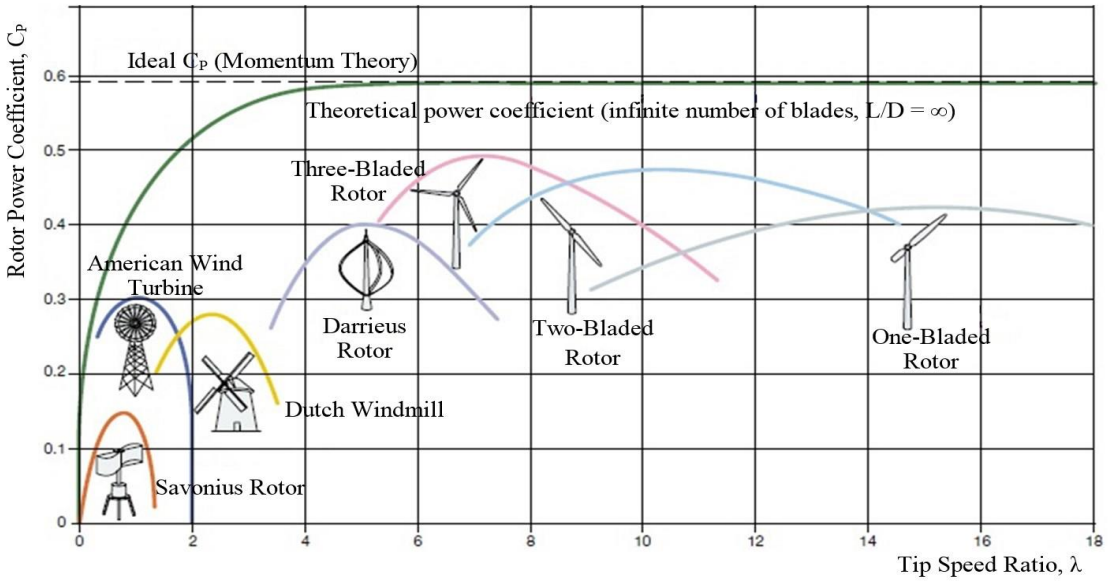

Figure 2.7 Power Coefficients for Different Rotor Designs[22]

2.3 Rotor design

2.3.1 Airfoil selection

Selecting an aerodynamic profile is essential to the rotor's design. In fact, it establishes the lift and drag coefficients, which in turn determine the wind turbine's aerodynamic performance. The NACA (National Advisory Committee for Aeronautics) airfoils are the most widely used among all types of airfoils. The four-digit code in the format NACA MPXX serves as the basis for defining these profiles, with:

- M: Maximum camber as a percentage of the chord,
- P: Maximum camber point relative to the leading edge as a percentage of the chord,
- XX: Maximum profile thickness as a percentage of the chord,

There are also five-digit NACA profiles that correspond to more complex load-bearing surfaces. Symmetrical profiles (MP = 00) are the most commonly used, although these produce a lower torque at start-up.

A study was carried out at the University of Windsor in Canada analyzing the performance of several airfoils for a Darrieus rotor [23]. Of all the profiles tested, the NACA0015 and NACA0018 were the best candidates in terms performance. Some asymmetrical profiles such as the NACA4415 or the NASA LS-0417 produce more torque at start-up, but the NACA0018 (Figure 2.8) is generally more efficient and suitable for low to moderate Reynolds numbers [24]. Moreover, many authors choose this same profile when it comes to studying VAWTs, [25, 26] and [27] consider it to be the ideal profile for this type of wind turbine. It is therefore this same profile that was used in this work.

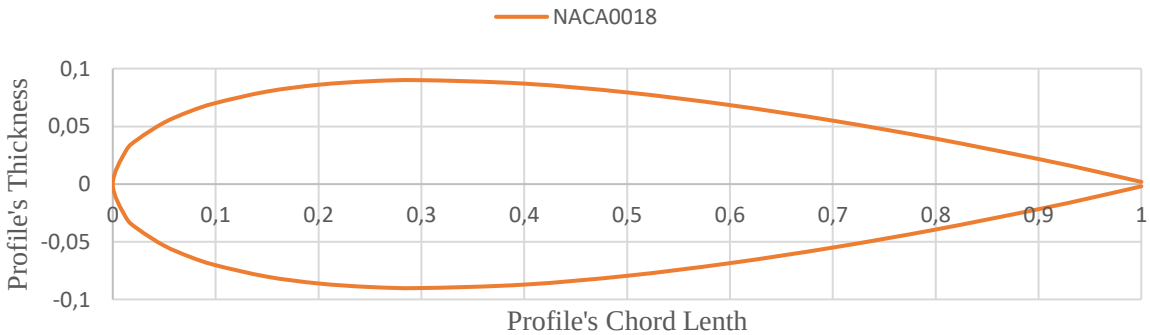

Figure 2.8 NACA 0018 Airfoil Generated by Q-blade Software

2.4 Conclusion

In conclusion, this chapter has introduced the key aerodynamic considerations essential for the performance of a Vertical Axis Wind Turbine. It represented the fundamental aerodynamic forces involved, including the key equations that describe lift, drag, and power production. The analysis also covered the theoretical limits of wind turbine efficiency, particularly through the Betz limit, which explains why turbines cannot exceed a maximum efficiency of 59%. Furthermore, the chapter highlighted the selection of NACA airfoils for the rotor, emphasizing their role in optimizing turbine performance by reducing drag and improving lift characteristics. A thorough understanding of these aerodynamic principles is crucial for enhancing VAWT efficiency, providing a foundation for ongoing design improvements and innovations in wind turbine technology.

CHAPTER 3:

CFD modeling

3.1 Introduction to CFD

The rapid advancement of computational technology and numerical methods has revolutionized the field of fluid dynamics, permitting detailed and precise analysis of complex flow phenomena. CFD (Computational Fluid Dynamics) has become an essential part of engineering design and an analytical environment for many companies that need the ability to evaluate new designs or processes, before they are manufactured or implemented as it provides a suitable and cost-effective approach to predict the aerodynamic performance, optimize designs, and predict real-world performance under various operating conditions. CFD solutions from ANSYS are based on the proven technology of Fluent software. The aerodynamic forces of the blade responsible for energy production must be increased in order to maximize efficiency. At the same time, the effects of these aerodynamic loads on the wind turbine components must be mitigated in order to extend the service life of the machine**.**

3.2 Literature review

In this section, the possible methods of analyzing a VAWT will be outlined followed by a detailed review of current research with a focus on CFD modeling as it will be the tool of analysis in this thesis.

3.2.1 Methods of VAWT analysis

The performance of a VAWT can be studied using a variety of methods. There are two primary categories: experimental and numerical methods. Figure 3.1 summarizes this process. While numerical analysis is carried out by modeling fluid phenomena, experimental analysis is carried out in wind tunnels. The two categories of numerical models are Computational Fluid Dynamics and Computational Aerodynamics. Despite being much faster than CFD models, aerodynamic models are inaccurate at predicting VAWT performance, particularly when the turbine is operating at low *TSR*s. Given that the resources required to perform CFD simulation can be too expensive, aerodynamic models seemed once the most popular modeling approach. However, with recent advances in computing, CFD simulations have become much more appealing. The Navier-Stokes equations are discretized and solved for CFD simulations, yielding far more accurate results; however, the cost and time of computation are increased.

Finally, Direct Numerical Simulation (DNS) is the most accurate and computationally expensive method. In DNS, the Navier-Stokes equations are fully resolved without any modeling, which results in a very high computational cost due to the extremely fine mesh and time step required. Xin et al. [28] provide Further details on most of the methods discussed here

, the authors have conducted relevant studies on Darrieus VAWTs. it should be noted that the RANS models presented here are the most widely used models for VAWT analysis.

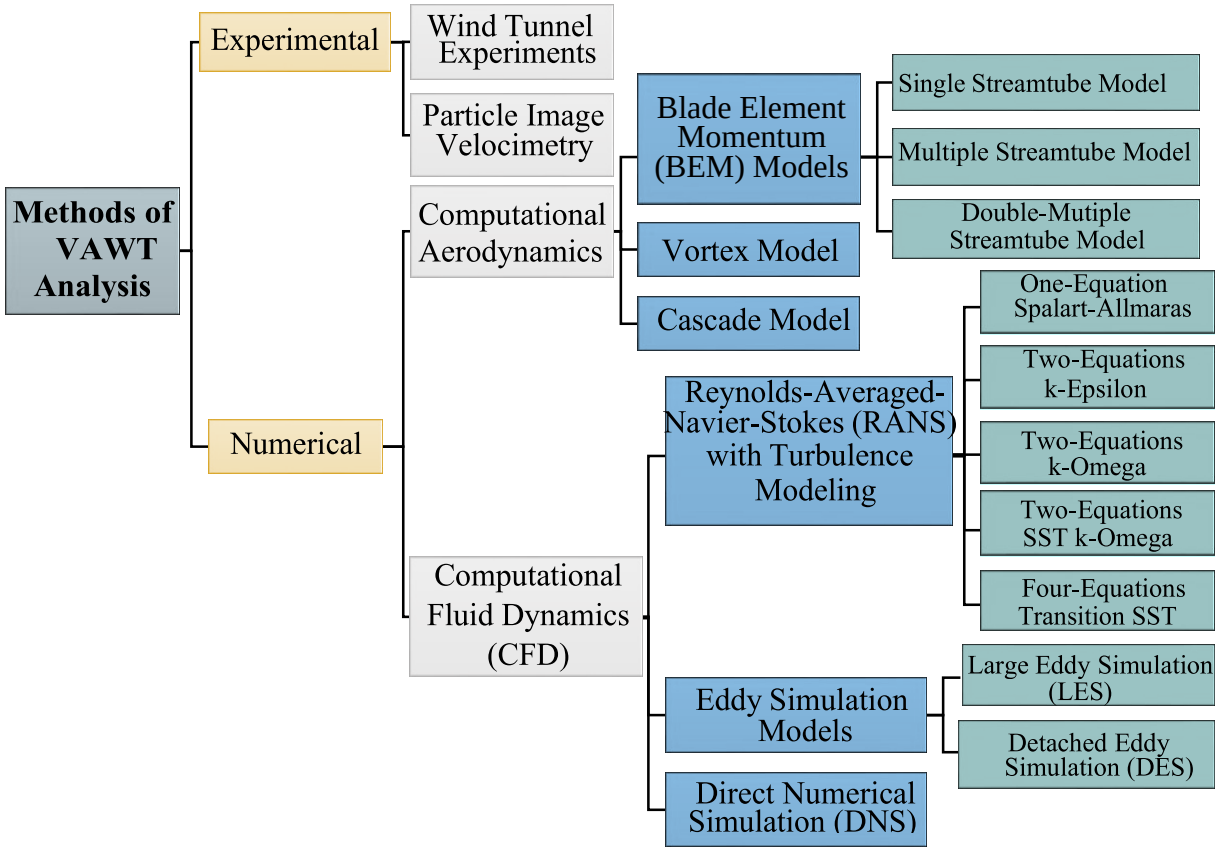

Figure 3.1 Summary of Methods for VAWT Analysis

3.2.2 Current research

This section reviews recent studies on Darrieus wind turbines, focusing on those employing CFD analysis, which forms the basis of the methodology used in this thesis. Special emphasis is placed on research specific to H-Darrieus turbines. Additionally, relevant advancements in Darrieus turbine research will be discussed to provide context for this study's objectives.

3.2.2.1 Study on high-solidity VAWTs

High-solidity Darrieus VAWTs have gained considerable attention for their capacity to efficiently harness medium to high wind speeds, with a design that increases blade surface area, allowing enhanced torque generation. Computational Fluid Dynamics (CFD) has emerged as an essential tool in optimizing these turbines, allowing detailed analysis of aerodynamic forces

such as lift, drag, and torque across varied wind conditions [29]. High-solidity VAWTs feature more substantial or numerous blades, creating a larger area for wind interaction and thus higher torque output, though this increase in solidity also leads to elevated drag forces at high speeds [30].

CFD simulations offer critical insights into the performance dynamics of high-solidity Darrieus turbines under medium to high wind speeds. According to Qamar & Janajreh [31]., CFD analysis reveals that lift forces become more dominant at higher *TSR* values, contributing to increased torque while also indicating a need to balance lift and drag for optimal efficiency. At higher *TSR*s, CFD studies have identified that although drag forces are more significant, they can be mitigated by optimizing blade design to maximize lift-driven torque generation across varying flow velocities [32].

Brusca et al. [33]. used CFD to explore the performance stability of high-solidity Darrieus VAWTs under turbulent wind conditions. Results indicated that higher solidity helps reduce fluctuations in rotational speed caused by wind turbulence, providing more consistent power output even in windy conditions. This stability, is critical for turbines deployed in environments with unpredictable wind patterns, making high-solidity Darrieus designs particularly advantageous for regions with medium to high average wind speeds.

Further CFD-based research by Balduzzi et al.[34], found that high-solidity Darrieus VAWTs can maintain efficiency across a wide range of wind speeds by balancing torque and drag forces to sustain steady power production. As such, CFD has become a fundamental method for analyzing VAWT designs for further enhancements, by allowing for precise modeling of aerodynamic interactions and facilitating design improvements for stable, reliable power generation.

3.2.2.2 CFD vs. Computational aerodynamics models

The Blade Element Momentum (BEM) theory is commonly used for analyzing the performance of lift-driven wind turbines, especially HAWTs. However, applying BEM to VAWTs presents specific challenges, primarily due to the unique aerodynamic behaviors of VAWTs. Unlike HAWTs, VAWTs experience a continuously changing *AoA* as their blades rotate around the central axis. This leads to unsteady aerodynamic conditions that complicate the assumptions underlying BEM theory.

BEM assumes steady flow and relatively uniform angles of attack across the turbine blades, making it less accurate for VAWTs, where the rotational motion induces highly variable angles of attack. As a result, the theory struggles to accurately predict performance in cases where aerodynamic phenomena such as stall and vortex shedding play a significant role. These complexities can lead to notable inaccuracies, as BEM does not account for the dynamic changes in lift and drag forces experienced by each blade throughout its rotation.

In contrast, CFD provides a robust framework for analyzing the performance of VAWTs by simulating fluid flows with high fidelity. CFD effectively models complex phenomena, such as turbulence and vortex interactions, and offers detailed insights into the fluid behaviors around turbine blades. Specifically, CFD simulations in computational aerodynamics enable precise tracking of airflow and pressure distributions, which is crucial for evaluating the aerodynamic performance of VAWTs.

Delafin et al. [35] compared the performance of a Darrieus turbine using both the double-multiple streamtube and vortex aerodynamic models against 3D RANS CFD simulations employing the SST k-ω turbulence model. The researchers found that the 3D simulations provided high fidelity and accurate predictions of the turbine's behavior, whereas the aerodynamic models consistently overestimated the power output across various *TSR*s. This clearly illustrates the enhanced accuracy that CFD can provide in capturing the intricate aerodynamic phenomena associated with turbine performance.

Ultimately, while BEM theory models turbine rotors by breaking them down into blade elements, it falls short for VAWTs, which are characterized by non-uniform aerodynamic behaviors. The variable angles of attack, unsteady flow conditions, and intricate stall patterns necessitate the use of CFD for more reliable and accurate performance analysis of VAWTs.

3.2.2.3 CFD approaches for H-Darrieus VAWT analysis

In order to simulate Darrieus VAWTs in 2D,Balduzzi et al. [34] compiled a list of frequently used approaches including the selection of the turbulence model, domain size, and cycle to cycle convergence criterion. Table 3.1 presents an overview of their findings. They have endorsed the SST k-ω model, $y+\sim 1$, and most importantly to have a convergence criterion for the torque variation from cycle to cycle of less than 0.1%, rather than the widely accepted value of 1%, after conducting their own investigation. They discovered that a 1% fluctuation can last for up to 10 cycles, resulting in a significant overestimation of the torque value.

Table 3-1 Comparative Analysis of the Literature Settings for 2D Unsteady Simulations of Darrieus Type [34]

Simulation settings								
Turbulence Model			**Algorithm**		**Azimuthal increment per time step**		**Revolutions to convergence**	
Spalart-Allmaras		[36]	**SIMPLE**	[37-40]	**$\Delta\theta \leq 0.5°$**	[41, 42]	**$Rev \leq 5$**	[37]
k- ε	**Standard**	[43, 44]						
	Realizable	[37, 45]			**$0.5° < \Delta\theta \leq 1°$**	[39, 45, 46]	**$5 < Rev \leq 10$**	[45, 46]
	RNG	[38, 47]	**Discretization scheme**					
k-ω	**Standard**		**1st order**	[38]	**$1° < \Delta\theta < 2°$**	[40]	**$10 < Rev \leq 15$**	[36, 39, 47]
	SST	[39]						
	SST-SAS	[48]	**2nd order**	[39, 41, 43, 47]	**$\Delta\theta = 2°$**		**$15 < rev$**	-
DES & LES		[42]						
Domain dimensions								
Inlet			**Outlet**		**Width**		**Rotating region**	
$L_1 \leq 5D$		[37, 38, 48]	**$L_2 \leq 10D$**	[37, 38, 48]	**$W \leq 5D$**	[39, 46]	**$D_{RR} \leq 1.2D$**	[43]
$5D < L_1 \leq 10D$		[46]	**$10D < L_2 \leq 20D$**	[37, 46]	**$5D < W \leq 10D$**	[38, 44]	**$1.2D < D_{RR} \leq 1.5D$**	[38, 48]
$10D < L_1$		[41, 45]	**$20D < L_2$**	[41, 45]	**$10D < W$**	[41, 45]	**$1.5D < D_{RR}$**	[41, 45]
Mesh								
y+			**Number of nodes on airfoil**		**Mesh size**		**Mesh type**	
~1	[39, 43, 44, 48]		**$N_N < 200$**	[38]	**$N_E \leq 2.5\times10^5$**	[37, 38, 43, 48]	**Structured**	[39]
$1 < y+ \leq 10$	[46, 47]		**$200 < N_N < 2000$**	[48]	**$2.5\times10^5 < N_E \leq 1.0\times10^6$**	[48 ,45]	**Unstructured**	[37, 45]
$30 < y+$	[37]		**$2000 < N_N$**	[42, 45]	**$1.0\times10^6 < N_E$**	[46]	**Unstructured with prismatic BL**	[36, 48]

The standard form of the SST k-ω and the SST k-ω with a correction for low Reynolds number effects were compared by McNaughton et al.[49] They tested the models for a turbine running at a Reynolds number of 150,000 in 2D with a $y+ < 1$. They demonstrated that the low Reynolds correction model improved performance prediction. In 2D with a $y+ < 1$, Lanzafame et al.[50] compared the four-equations Transition SST model with the two-equations SST k-ω. Although the Transition SST model is more computationally expensive and requires a number of tests to calibrate the local correlation parameters with the experimental values in order to obtain accurate results, it demonstrated a significantly higher degree of agreement with experimental results than the SST k-ω.

Ferreira et al.[42] compared the experimental results from Particle Image Velocimetry (PIV) with the simulation results in 2D for turbine cases where dynamic stall occurred. They discovered that the DES model, the LES model, and the two URANS models, the SA and the k-ε model, agreed with their experimental results the best. These outcomes were anticipated because Eddy models are known to be more accurate, but they also have the disadvantage of requiring more computing power.

3.3 Governing equations

CFD simulations are performed by solving the discretized Navier-Stokes equations. However, if one wants to solve the entire Navier-Stokes equations using DNS simulations, the computational cost will very expensive. Rather, the Reynolds Averaged Navier-Stokes (RANS)

time averaged equations are solved, providing sufficient accuracy for the majority of engineering applications.

The flow is usually taken to be incompressible for VAWT analysis since it simplifies the equations without affecting accuracy. For Newtonian fluids, the robust formulation of the incompressible and unsteady Navier-Stokes equations is:

$$\nabla.\vec{u} = 0 \tag{40}$$

$$\rho\frac{\partial\vec{u}}{\partial t} + \rho(\vec{u}.\nabla)\vec{u} = -\nabla.p + \mu\nabla^2\vec{u} + f \tag{41}$$

Where $\vec{u}$ is the velocity vector, μ is dynamic viscosity and f is body forces. The instantaneous flow fields such as velocity and pressure are decomposed into mean and fluctuating components such as:

$$u_i = \overline{u_i} + u_i' \tag{42}$$

$$p = \overline{p} + p' \tag{43}$$

Where u_i and p are the instantaneous velocity and pressure components, u_i and p are the mean velocity and pressure components, and u_i' and p' are the fluctuating velocity and pressure components. The components of mean and fluctuating pressure and velocity vary over time and space. The subscript i = 1, 2 and 3 refers to the each of the components along the x, y, and z direction, respectively. Using some mathematical manipulation and the above-mentioned formulation, the RANS equation in conservative form are given by the following:

$$\frac{\partial U_i}{\partial x_i} = 0 \tag{44}$$

$$\rho\frac{\partial U_i}{\partial t} + \rho\frac{\partial}{\partial x_j}\left(U_iU_j + \overline{u_i'u_j'}\right) = -\frac{\partial P}{\partial x_i} + \frac{\partial}{\partial x_j}(2\mu S_{ij}) \tag{45}$$

Where $-\overline{u_i'u_j'}$ is the average of the product of the velocity fluctuations in the i and j directions, $-\overline{u_i'u_j'} = \tau_{ij}$, is called the specific Reynolds Stress tensor, U_i is the mean velocity in the i direction, and S_{ij} is the strain rate tensor:

$$S_{ij} = \frac{1}{2}\left(\frac{\partial u_i}{\partial x_j} + \frac{\partial u_j}{\partial x_i}\right) \quad (46)$$

Based on the Boussinesq approximation, the specific Reynolds Stress tensor can be expressed as a product of eddy viscosity, v_t, and local mean flow strain rate.

$$-\rho\overline{u_i' u_j'} = \rho v_t \left(\frac{\partial U}{\partial y} + \frac{\partial V}{\partial x}\right) \quad (47)$$

After simplifying the Navier-Stokes equations in conservation form, the more common expression for the RANS equation is obtained.

$$\rho\frac{\partial U_i}{\partial t} + \rho U_j \frac{\partial U_i}{\partial x_i} = -\frac{\partial P}{\partial x_i} + \frac{\partial}{\partial x_j}\left(2\mu S_{ij} - \rho\overline{u_i' u_j'}\right) \quad (48)$$

The system is not yet closed because there are more unknown variables than equations to solve in the above form. The goal of turbulence modeling is to solve for the eddy viscosity variable, which connects the RANS equation with the turbulence model equations using the Boussinesq approximation, and to find enough equations to solve for all the unknowns. The turbulence model equations are presented in the following subsections.

3.4 Turbulence modelling

The two-equation Shear-Stress Transport (SST) k-ω model [51, 52] has a similar form to the standard k-ω model (turbulent kinetic energy-specific dissipation rate). It combines the benefits of the k-ε model in free flow with the advantages of the standard k-ω for near wall flows. The governing equations are given by the following [53] :

$$\frac{\partial(\rho k)}{\partial t} + \frac{\partial(\rho k u_j)}{\partial x_j} = \frac{\partial}{\partial x_j}\left(\Gamma_k \frac{\partial k}{\partial x_j}\right) + \widetilde{G_k} + -Y_k + S_k \quad (49)$$

And :

$$\frac{\partial(\rho\omega)}{\partial t} + \frac{\partial\left(\rho\omega u_j\right)}{\partial x_j} = \frac{\partial}{\partial x_j}\left(\Gamma_\omega \frac{\partial \omega}{\partial x_j}\right) + G_\omega - Y_\omega + D_\omega + S_\omega \quad (50)$$

Where $\widetilde{G_k}$ is the generation of turbulence kinetic energy due to the mean velocity gradients, G_ω is the generation of ω, Y_k and Y_ω are the dissipation of k and ω due to turbulence,

D_ω is the cross-diffusion term, and S_k and S_ω are the user-defined source terms. Γ_k and Γ_ω are the effective diffusivities of k and ω, and are calculated using the following equations:

$$\Gamma_k = \mu + \frac{\mu_t}{\sigma_k} \quad (51)$$

$$\Gamma_\omega = \mu + \frac{\mu_t}{\sigma_w} \quad (52)$$

Where σ_k and σ_w are the turbulent Prandtl numbers for k and ω, respectively. μ_t is the turbulent viscosity called by the following:

$$\mu_t = \frac{\rho k}{\omega} \frac{1}{max\left(\frac{1}{\alpha^*}, \frac{SF_2}{\alpha_1 \omega}\right)} \quad (53)$$

Where S is the Strain rate magnitude. The rest of the equations and closure variable are available in ANSYS Fluent's Theory guide [53].

3.5 Wall treatment

The law of the wall is shown in Figure 3.2, which is the velocity profile in the near-wall region based on a semi-empirical formula. One can see that profile is composed of three regions in the inner layer, which are defined by the dimensionless distance, y^+. The three regions are the log law region, buffer region and viscous sublayer. The y^+ is defined as:

$$y^+ = \frac{\rho u_\tau y}{\mu} \quad (54)$$

With:

$$u_\tau = \sqrt{\frac{\tau_w}{\rho}} \quad (55)$$

Where u_τ is the friction velocity and y is the normal distance from the wall.

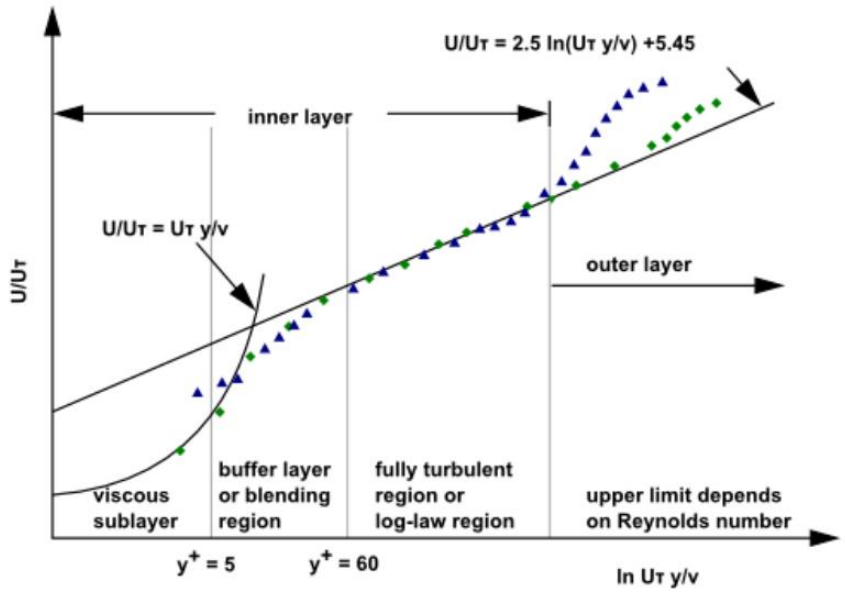

Figure 3.2 Sub-Divisions of the Near-Wall Region [53]

There are two commonly used approaches for modeling the flow near walls. The semiempirical formulas known as wall functions serve as a link between the free stream flow and the extremely viscous flow in the boundary layer. For the smallest element, the usual range is $y^+ > 30$, where the wall functions are used to calculate the flow and its properties below that y^+. The flow degrades and unbound errors occur if a mesh with elements smaller than y^+ of 15 is used [53]. With the second approach, the flow is resolved all the way to the wall, including the viscous sublayer. Although a much finer mesh is obviously needed to capture the flow details, the flow prediction accuracy is usually higher.

The Enhanced Wall Treatment (EWT), which is Fluent's default wall treatment for the previously described turbulence model, is applied to all simulations conducted for this thesis. Because it combines the behavior of the two previously mentioned approaches, the Enhanced Wall function has a wide range of applications. It permits the use of coarse meshes, in which the flow will be resolved to the smallest element. The wall function will then take over and approximate the effects below that smallest element. However, the flow will be fully resolved without the wall function being activated if the mesh is fine enough (below $y^+ < 1$). Therefore, EWT performances can be considered as independent of y^+.

3.6 Numerical setup

3.6.1 Turbine geometry

The currently analyzed design mainly consists of 3 aerodynamic profile blades attached to a vertical rotating shaft, which is not included in the geometrical model to reduce computational complexity, as shown in Figure 3.3.

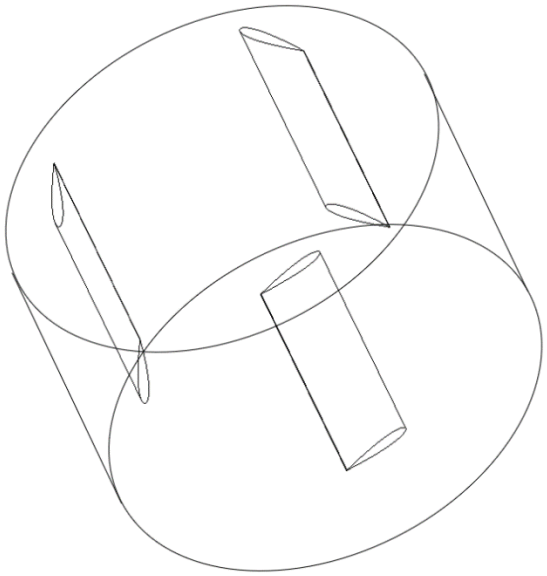

Figure 3.3 Schematic view of the turbine geometry used for CFD simulation

As reported in Table 3-2, the design parameters and dimensions of the geometric model employed in this work are inspired by the dimensions of an H-Darrieus VAWT that was experimentally tested by Elkhoury et al. [54].

Table 3-2Design Parameters of the H-Darrieus Wind Turbine

Parameter	***Value***
Rotor Diameter D (**m**)	2.00
Blade Airfoil	NACA 0018
Blade Shape	Straight
Chord Length c (**m**)	0.5
Rotor Height H (**m**)	2.00
Blades Number N	3
Solidity $\boldsymbol{\sigma}$ $(-)$	0.75

3.6.2 Computational domain

Two domains of interest can typically be taken into account for H-Darrieus wind turbine CFD simulations: a rotating domain that accounts for the rotor and a fixed domain that represents the control volume. A 50 m × 20 m rectangle serves as the fixed domain in this work, while a 4 m or 2D diameter circle serves as the rotating domain (Figure 3.4). It is evident that the rotor's center was situated 10 degrees from the inlet boundary and 15 degrees from the outlet boundary. This was established to guarantee proper wake effect development[55], which could result in an overestimation of turbulence and an underestimation of fluid velocity [56].

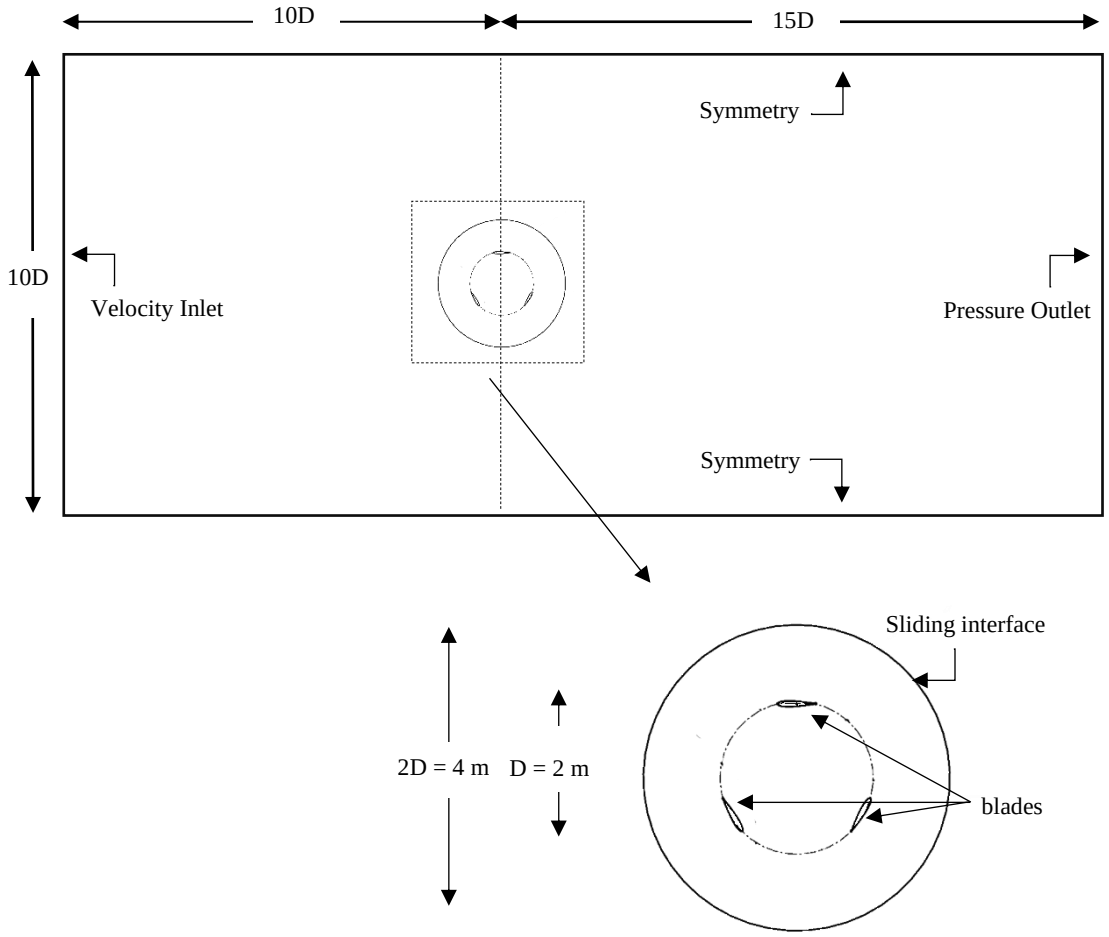

Figure 3.4 Schematic View of the Computational Domain and Boundary Conditions

3.6.3 Fluent set-up

For the Unsteady Reynolds-Averaged Navier-Stokes (URANS) calculations, the pressure-based solver was selected due to its efficiency in handling incompressible and low-speed compressible flows, which are typical in VAWT applications. The pressure-velocity

coupling was managed using the coupled algorithm, which offers enhanced stability and convergence.

The second-order upwind scheme was employed for spatial discretization of pressure, turbulence, and momentum equations to improve solution accuracy, particularly in capturing gradients associated with turbulence and rapidly changing flow conditions around the turbine blades. This higher-order discretization scheme is critical in VAWT modeling as it provides more precise solutions by reducing numerical diffusion, which can otherwise lead to an underestimation of turbulence effects. The main settings implemented for all simulations, are detailed in Table 3-3.

Table 3-3 Details of Fluent Set-Up that was Employed in this Work

Parameter	***Symbol***	***Value***
Turbulence Model	SST k- ω	/
Air Density	ρ	$1.225\ kg/m^3$
Air viscosity	μ	1.79×10^{-5} Pa s
Air Velocity	U_∞	$8\ m/s, 20 m/s$
Turbulent Intencity		1%
Tip Speed Ratio	λ	0.4-1.5
Solver Type		Pressure-Based
Calculation Algorithm		Coupled
Spatial Discretization		2nd
Time Discretization		According to λ=1, calculated to achieve 2˚ of rotation per timestep
Risiduals		1×10^{-4}

3.6.4 Mesh generation

The computational mesh used in this study was generated using ANSYS 24.2 Design Modeler meshing tool. In order to find the optimal mesh size in terms of accuracy and computational cost, the impact of the computational grid on the primary computations was assessed.

For a fixed wind speed of 8 m/s and a *TSR* of 1, three distinct unstructured computational meshes were tested in this investigation. After this analysis, the medium mesh was determined to be the optimal option among all tested meshes. After testing the finest mesh, it was found that the average power coefficient value difference was less than 1.26%. For every mesh, the number of elements in the computational domains and their corresponding average C_p values are shown in Table 3-4.

Table 3-4 Details of Mesh Independence Test for λ = 1

		Mesh Set		
		Coarse	***Medium***	***Fine***
Face Sizing	Fixed Domain Element Size (m)	0. 30	0. 20	0. 15
	Rotor Domain Element Size (m)	3.0×10^{-2}	1.83×10^{-2}	1.33×10^{-2}
Edge Sizing	Interface Element Size (m)	2.27×10^{-2}	1.73×10^{-2}	1.23×10^{-2}
	Number of Divisions around blade surface	400	500	600
Boundary Layer	First Layer Height (m)	5×10^{-4}	5×10^{-4}	5×10^{-4}
	Number of elements	15	20	25
	Growth Rate	1.2	1.2	1.2
Number of Elements	Fixed Domain	54089	200660	340101
	Rotor Domain	161764	151753	257209
	Total	215853	352413	597310
Power Coefficient	C_p	0.194	0.201	0.204
	Difference of C_p with respect to the Fine Mesh (%)	– 4.9	–1.47	/

The three meshes taken into consideration in this study were sized using similar methods, which are as follows :

- First, the triangles method was applied for both domains,
- Next, face sizing was used to refine the rotating domain,
- Following this step, using edge sizing, the interface between the rotating domain and the fixed domain was refined,
- Finally, the surfaces of the blades were grid sized by increasing the number of surrounding elements and generating an adequate inflation number for each one. This was done to ensure a $y^+ < 1$,

This approach was considered to capture the viscous sublayer, as suggested by [34]. It is important to mention that the selected medium mesh size (Figure 3.5), complies with two conditions:

- the 0.22 lowest orthogonal quality for the whole mesh is larger than 0.
- the 0.79 maximum skewness for the whole mesh is smaller than the 0.95 maximum as advised by[53].

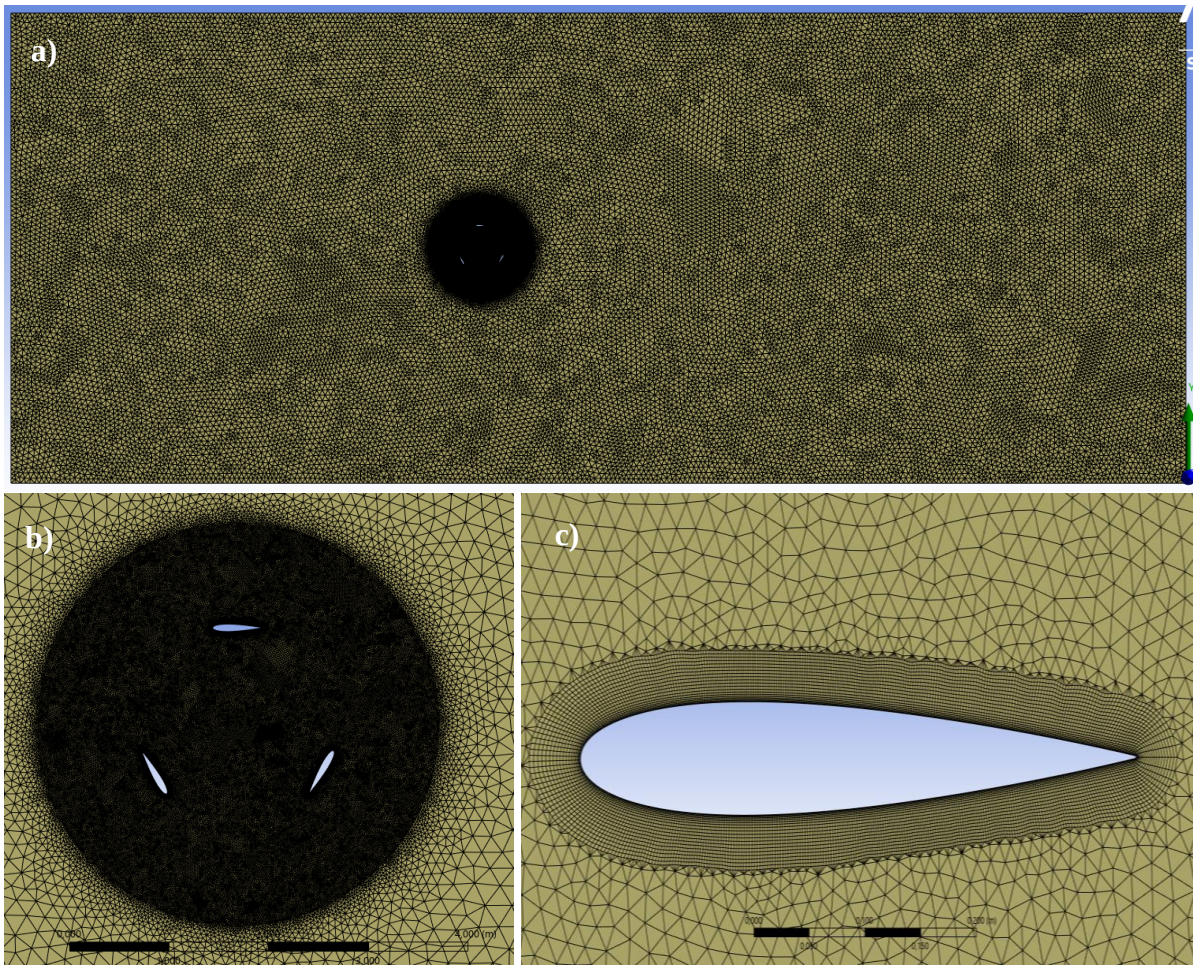

Figure 3.5 Medium Mesh Detailed Grids: (a) Grids in the Entire Computational domain, (b) Grids in the Rotating Domain, (c) Grids Around Blade 1

3.6.5 Angular marching step

The timestep size is a crucial parameter in the development of unsteady simulations as it significantly affects the results that are obtained [57]. This was carried out by evaluating three different time steps over 10 consecutive rotations, using the simulation for U_∞ = 8 m/s at λ = 1 as the base case, which corresponds to an angular velocity of 8 rad/s. Finding the right time step Δt to generate the most consistent C_p results at the lowest computational cost was considered to be an effective approach. Therefore, 0.008753 s, 0.004376 s, and 0.002188 s were the three timesteps evaluated for the base case. These timesteps correlated to angular marching steps $\Delta\alpha$ of 4˚, 2˚, and 1˚, respectively.

Figure 3.6 showed that the C_p value stabilization required a different number of simulated rotations for each $\Delta\alpha$. This is the case when $\Delta\alpha$ = 4˚, which requires the fewest. Conversely, even though it took more simulated rotations to achieve stable C_p values when $\Delta\alpha$ = 2˚ than when $\Delta\alpha$ = 4˚, its final C_p value only differed by 3.10% from the C_p value determined when

$\Delta\alpha = 1^{\circ}$. Thus, $\Delta\alpha = 2^{\circ}$ was considered to be a good compromise, as reported in Table3-5, lowering computational costs without significantly affecting the accuracy of the results.

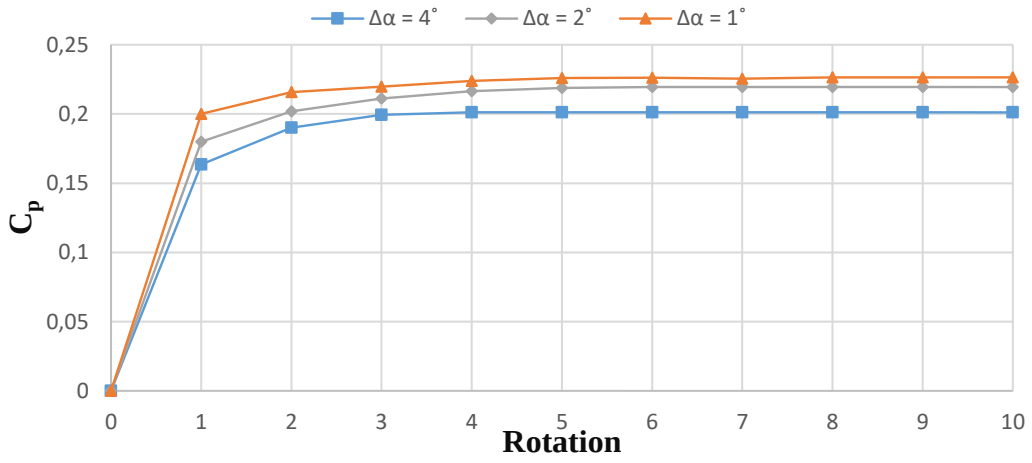

Figure 3.6 Power Coefficient Changes with the Number of Rotations for U_{∞} = 8 m/s when adopting Different $\Delta\alpha$ at λ=1

Table 3-5 Timestep Independence Test for λ = 1

Time Step Δt (s)	***Angular Marching Step Δα (°)***	***Cm***	***Cp***	***Difference of Cp with Respect to Smallest Time Step (%)***
0.008753	4	0.201	0.201	-11.06
0.004376	2	0.219	0.219	-3.10
0.002188	1	0.226	0.226	/

3.7 Conclusion

In conclusion, this chapter presented the CFD methodology applied to simulate the aerodynamic behavior of Vertical Axis Wind Turbines. CFD modeling, specifically using ANSYS Fluent, was shown to offer a more detailed view of aerodynamic interactions than simpler models like Blade Element Momentum theory. This approach centered on turbulence modeling with the k-omega SST model, well-suited for accurately representing turbulent flows around turbine blades. Additionally, the chapter highlighted practices for effectively resolving the boundary layer around the blades, focusing on mesh strategies to maintain a balance between computational cost and simulation accuracy. This methodology forms a solid basis for examining VAWT performance, allowing detailed analysis within reasonable computational limits and setting the foundation for the results in the following chapter.

CHAPTER 4:

Results and discussions

4.1 Model validation

To validate the 2D CFD simulations of the H-Darrieus wind turbine carried out in this work, the calculated average C_p values were compared with the values reported by Ma et al. [57], at various *TSR*s. In their study, the authors used 3D CFD simulations and wind tunnel experiments to assess the same rotor configuration for a wind speed U_∞ = 8 m/s. However, at a significantly lower computational cost than 3D and even 2.5D simulations, 2D simulations can offer a dependable representation of the flow in the turbine's mid-plane, despite the possibility of some discrepancies with regard to the experimental results [58]. Table 4-1 reports the differences between the experimental data and the results of each type of CFD simulation.

The average C_p values predicted by simulations for a 2D model were consistently higher than those derived from 3D simulations, as shown in Figure 4.1. The complex interactions and flow dynamics around the wind turbine blades are only partially captured in 2D simulations, which can lead to limitations in accuracy [50, 59]. For *TSR*s between 0.4 and 0.9, the average relative error was around ±9.35%, with a maximum error of 22.66%. This suggests that the 2D model can reliably capture the general performance trends of the turbine, particularly at *TSR* values below 0.9, offering a reasonable degree of accuracy when compared with experimental data.

However, for *TSR* values greater than 0.9, the simplifications inherent in the 2D model appear to reduce its accuracy in representing real-world performance, so these data points were excluded from the current analysis. As a result, the 2D simulation approach is considered appropriate for identifying performance trends, such as average C_p, torque generation, and overall efficiency, within the expected margin of error for *TSR* values below 0.9. This analysis provides a practical framework for testing and optimizing turbine performance across relevant operational ranges.

Table 4-1 Power Coefficient Comparison of 2D SST k-ω Simulation with Experimental Data and 3D Simulation

	Power Coefficient				
λ	***2D SST k- ω (This Work)***	***Experimental Results [57]***	***Relative Error 2D vs Exp (%)***	***3D SST k-ω [57]***	***Relative Error 3D vs. Exp (%)***
0.4	0.029	0.028	3.57	0.030	5.50
0.5	0.038	0.040	– 5.00	0.048	19.60
0.7	0.066	0.073	–9.59	0.079	8.60
0.8	0.107	0.101	5.94	0.105	4. 70
0.9	0.157	0.128	22.66	0.132	3.10
1.0	0.219	0.167	25.15	0.159	– 4.70
1.2	0.323	0.190	70.00	0.184	– 3.30
1.3	0.352	0.195	80.51	0.191	– 2.00
1.4	0.363	0.186	95.16	0.191	2.50
1.5	0.383	0.169	126.62	0.180	6.00

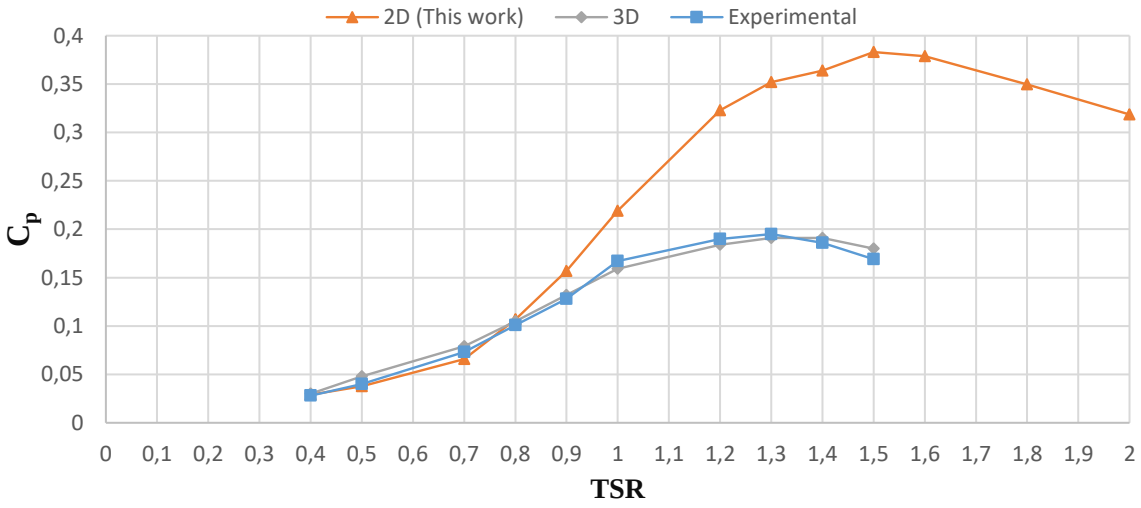

Figure 4.1 Comparison of Power Coefficient Changes vs TSR for 2D, 3D [57] and Experimental [57] at U_∞=8 m/s

4.2 Influence of wind speed

4.2.1 Wind Speed effect on overall torque

The average rotor overall torque values for both low (8 m/s) and high (20 m/s) wind speeds were consistent after two consecutive revolutions, which indicates that the stability criteria was achieved. For all the *TSR*s examined, as specified by[60], a difference of less than 1% in the average torque value between two subsequent rotations was obtained, as seen in Figure 4.2. In this regard, when the wind speed increased from 8 m/s to 20 m/s, the average rotor overall torque values showed a notable increase of roughly 5 to 7 times. The average rotor overall torque varied between 4.77 Nm for λ = 0.4 and 12.93 Nm for λ = 0.9 in the U_∞ = 8 m/s

simulations (Figure 4.2a) and 29.69 Nm for λ = 0.4 and 73.51 Nm for λ = 0.9 in the U_∞ = 20 m/s simulations (Figure 4.2b).

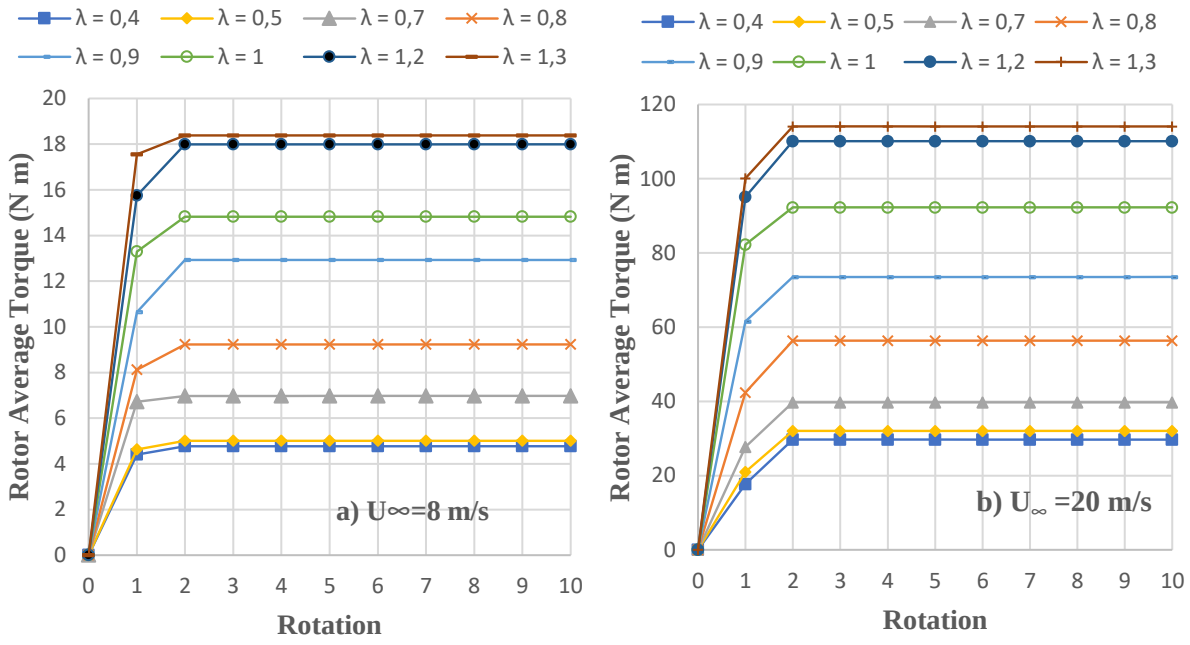

Figure 4.2 Average Rotor Overall Torque vs Rotation at Various TSRs for (a) U_∞ = 8 m/s and (b)U_∞ = 20 m/s Using the Previously Presented 2D Model

4.2.2 Wind Speed effect on drag and lift forces

The cyclic aerodynamic forces that occur during VAWT operation can lead to fatigue and low power coefficients C_p in contrast to those found in HAWTs.

The drag and lift forces on the three blades of the H-Darrieus wind turbine are shown in Figures 4.3 and 4.4 for two distinct *TSR*s (λ = 0.5 and λ = 0.9) at the same wind speed (U_∞ = 8 m/s). Additionally, these figures depict not only the displacements of these aerodynamic forces' maximum and minimum values, but also the changes in their cyclical behavior over a rotational period, both in terms of magnitude and distribution.

Then, it is evident that in at λ = 0.5 (Figure 4.3a) the maximum and minimum values for drag force, on the main blade are reached at θ = 60˚ and θ = 176˚, respectively. At λ = 0.9 (Figure 4.3b), there is a peak displacement, and these values are reached at θ = 84˚ and θ = 162˚, respectively. However, in the case of lift force, the displacement effect is small, blade1 reaches its maximum and minimum values at θ = 118˚ and θ = 50˚, respectively, when λ = 0.5 (Figure 4.4a) and at θ = 114˚ and θ = 54˚, respectively, when λ = 0.9 (Figure 4.4b). Hence, it can be observed that at higher λ, the drag forces on the blades increase significantly

(Figure 4.3). Moreover, in the case of the lift forces (Figure 4.4), an effect of λ on the second negative peak of the distribution in the azimuthal range of $\theta = 60^\circ$–180° is evidenced. One can see that this second minimum (-36 N) is reached at a prior azimuthal angle, as compared to the angle reached when $\lambda = 0.5$ (-16 N).

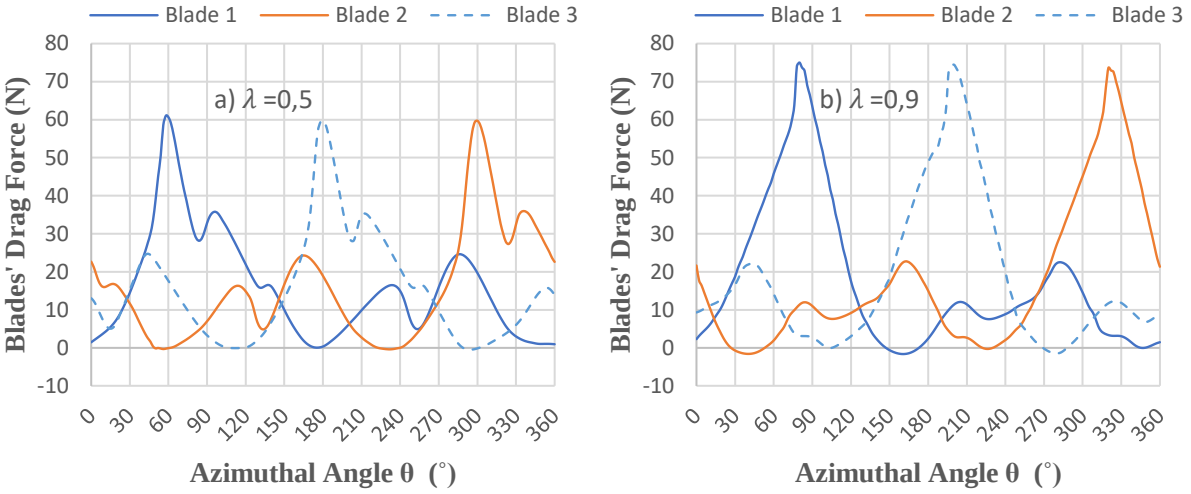

Figure 4.3 Drag Force for Each Blade vs Azimuthal Angle, for U_∞ = 8 m/s at (a) λ = 0.5 and (b) λ = 0.9 Using the Previously Presented 2D Model

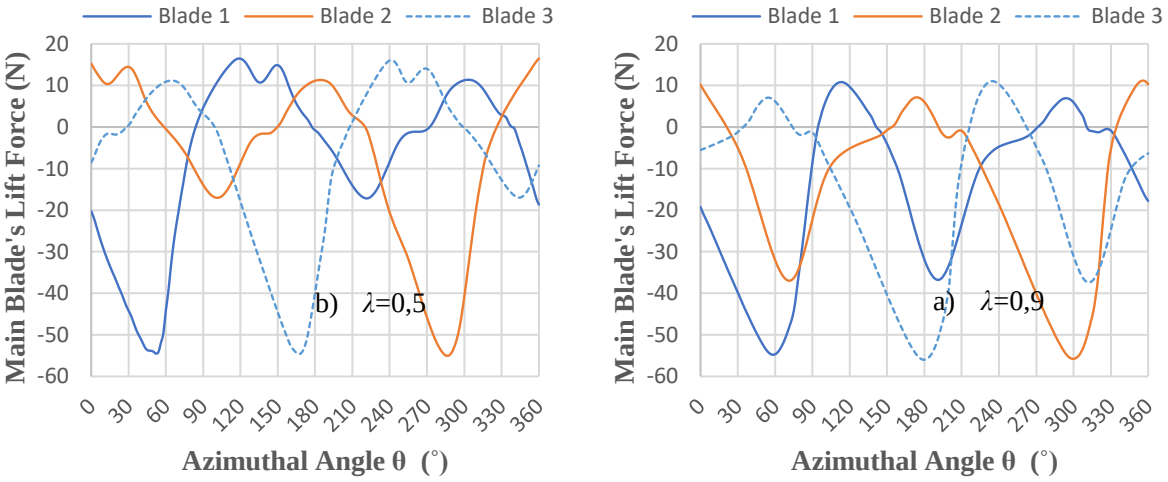

Figure 4.4 Lift Force for Each Blade vs Azimuthal Angle, for U_∞ = 8 m/s at (a) λ = 0.5 and (b) λ = 0.9 Using the Previously Presented 2D Model

On the other hand, a comparison of the main blade's drag force (Figure 5) and lift force (Figure 6) at both wind speeds reveals nearly identical distributions, with the main blade's maximum and minimum values of these two forces being reached roughly at the same azimuthal angles.

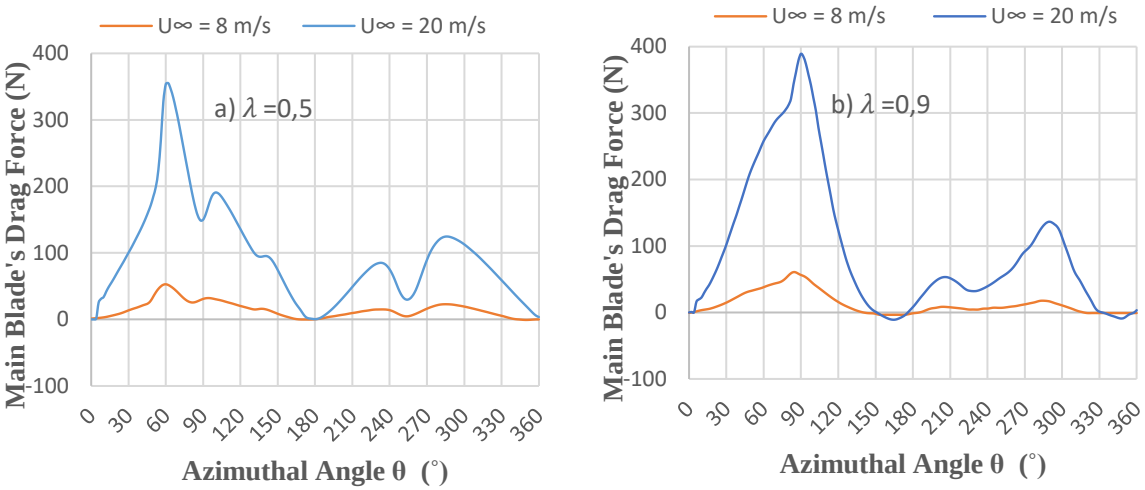

Figure 4.5 Drag Force for Blade 1 vs Azimuthal Angle, for U∞ = 8 m/s and U∞ = 20 m/s at:(a) λ = 0.5 and (b) λ = 0.9, the Using the Previously Presented 2D Model

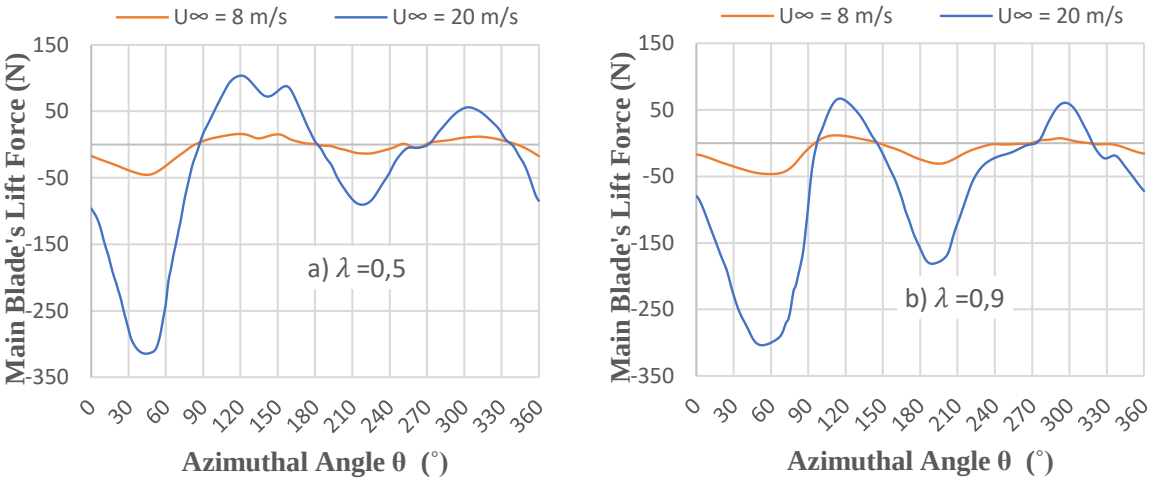

Figure 4.6 Lift Force for Blade 1 vs Azimuthal Angle, for U_∞ = 8 m/s and U_∞ = 20 m/s at:(a) λ = 0.5 and (b) λ = 0.9, Using the Previously Presented 2D Model

In the case of a fixed pitch blade, 'static stall' conditions are reached, as the *AoA* increases, and drag forces being greater than lift forces.

However, a pitching oscillation of the blades is caused by VAWT's rotation leads to a "dynamic stall" condition. As the *AoA* rapidly changes, this condition is characterized by the generation of a vortex that starts at the blade's leading edge and eventually sheds, with fluctuating lift and drag forces [61]. Therefore, the *AoA* α on each blade affects drag and lift forces as the wind turbine rotates, reaching various azimuthal angles. It is possible to characterize how *TSR* and azimuthal position *θ* affect *AoA* α (Equation (9)).

Then, When the main blade (Blade 1) begins to rotate counterclockwise from the $\theta = 0^{\circ}$, a 'dynamic stall' effect appears to start developing, with lift forces gradually decreasing and drag forces gradually increasing. For Blade 1, the lift force magnitude changes from −53 N for U_{∞} = 8 m/s to −311 N for U_{∞} = 20 m/s, according to Figure 4.6a. The lift and drag force minimum and maximum values occur between $\theta = 50^{\circ}$ and $\theta = 64^{\circ}$. Figure 4.6b shows that when λ increases from 0.5 to 0.9, this azimuthal angle does not significantly change. In addition, and at the same conditions, drag forces on Blade 1 show a peak increase from 54 N for U_{∞} = 8 m/s to 253 N for U_{∞} = 20 m/s (Figure 4.5a), when λ increases from 0.5 to 0.9 the drag force reachs 388 N for U_{∞} = 20 m/s (Figure 4.5b).

The maximum and minimum drag and lift forces for Blade 1 along with their corresponding angles of attack for both U_{∞} = 8 m/s and U_{∞} = 20 m/s at the two λ of interest are summarized in Table 4.2. Based on this, it is evident that when the *TSR* increases from 0.5 to 0.9, the maximum position of the drag forces for U_{∞} = 8 m/s changes from $\theta = 60^{\circ}$ to $\theta = 84^{\circ}$.this change can also be observed for U_{∞} = 20 m/s, with the maximum drag force position shifting from $\theta = 64^{\circ}$ to $\theta = 90^{\circ}$. In context of the lift forces, the displacement effect is insignificant, the maximum lift force peaks for Blade 1 for both wind speeds are at λ = 0.5 and λ = 0.9, in the azimuthal range of $\theta = 118^{\circ}$–120° and $\theta = 114^{\circ}$–116° respectively.

Table 4-2 Summary of Maximum and Minimum Lift and Drag Forces on the Main Blade for U_{∞} = 8 m/s and U_{∞} = 20 m/s at both λ = 0.5 and λ = 0.9

	λ	θ (°)	α (°)	
Figure 4.3 Drag Forces U_{∞} = 8 m/s	0.5	61	41.60	Maximum Drag
		176	–7.98	Minimum Drag
	0.9	84	44.71	Maximum Drag
		163	–79.10	Minimum Drag
Figure 4.4 Lift Forces U_{∞} = 8 m/s	0.5	49	33.14	Minimum Lift
		117	87.04	Maximum Lift
	0.9	55	29.07	Minimum Lift
		115	62.22	Maximum Lift
Figure 4.5 Drag Forces U_{∞} = 20 m/s	0.5	64	43.76	Maximum Drag
		182	4.00	Minimum Drag
	0.9	91	42.57	Maximum Drag
		164	–77.67	Minimum Drag
Figure 4.6 Lift Forces U_{∞} = 20 m/s	0.5	50	33.83	Minimum Lift
		120	90.00	Maximum Lift
	0.9	54	28.50	Minimum Lift
		115	62.22	Maximum Lift

4.2.3 Wind speed effect on individual torque

Regarding the torque values obtained on each blade of the H-Darrieus wind turbine, one can see that, for U_∞ = 8 m/s, the three blades present a cyclic pattern at both λ = 0.5 and λ = 0.9 (Figure 4.7), with the torque corresponding to the individual blade positions at various azimuthal angles. The peak torque values for each blade show an azimuthal angle difference of almost 26˚ when λ increases from 0.5 to 0.9. Depending on the rotor position, this can be attributed to the significant change in each blade's angle of incidence.

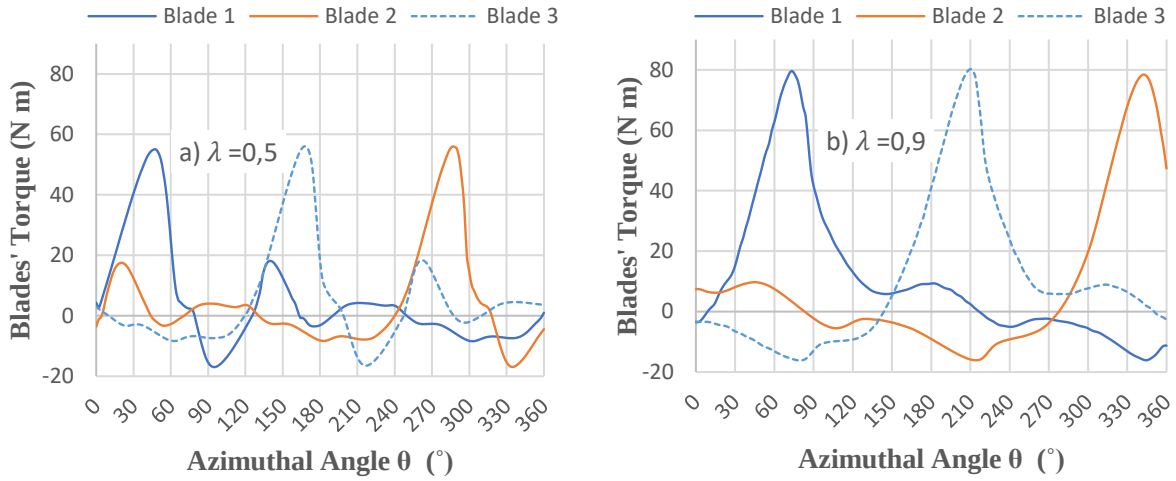

Figure 4.7 Torque on Each Blade vs Azimuthal Angle, for U_∞ = 8 m/s at: (a) λ = 0.5 and (b) λ = 0.9, Using the Previously Presented 2D Model

Based on this, it is feasible to consider how a rotor speed increase would cause the torque on the blades to increase and their peaks to shift. Additionally, it is evident from comparing the torque behavior on Blade 1 for a full rotor rotation using both U_∞ = 8 m/s and U_∞ = 20 m/s (Figure 4.8) that the main blade's maximum and minimum torque values are reached at close θ values for both wind speeds. Torque values produced at U_∞ = 20 m/s are also seven times greater than those produced at U_∞ = 8 m/s.

However, at higher wind velocities, one can anticipate both oscillations and a significant torque increase, as the peak and low torque distribution functions for both U_∞ present a similar trend. For a U_∞ = 20 m/s at λ = 0.5 (Figure 4.8a), on the other hand, Blade 1 maximum and minimum torque values are attained at θ = 50˚ (α = 33.8˚) and θ = 100˚, respectively. The minimum torque shifts to θ = 316˚ for U_∞ = 20 m/s at λ = 0.9 (Figure 4.8b), while the maximum torque is attained at θ = 78˚ (α = 41.4˚).

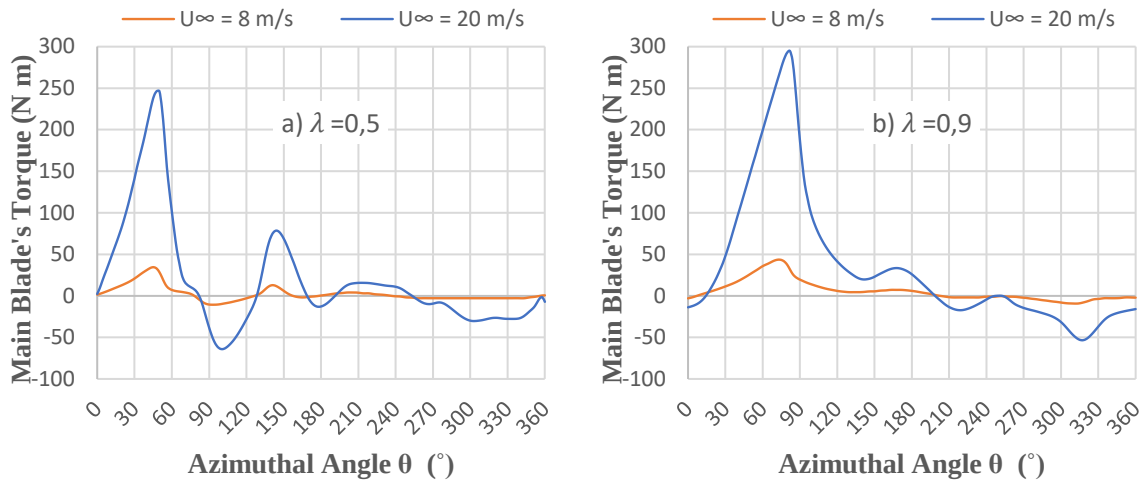

Figure 4.8 Torque on Blade 1 vs Azimuthal Angle, for U_∞ = 8 m/s and U_∞ = 20 m/s at (a) λ = 0.5 and (b) λ = 0.9, Using the Previously Presented 2D Model

By linking the maximum torque on Blade 1 (Figure 4.7) to its peak drag force position (Figure 4.5), Given that Blade 1 is in the θ = 0˚ to θ = 60˚ azimuthal position range under dynamic stall conditions, it can be concluded that drag forces have a greater impact on the torque peak than lift forces. This is true for U_∞ = 20 m/s as well, and the highest torque values are achieved at θ = 50˚ and θ = 78˚ (Figure 4.8). Likewise, Blade 1 will experience lift force vectors influenced by an asynchronous system of forces that affect torque and power when it is in the θ = 60˚ to θ = 120˚ azimuthal position range. For an H-Darrieus wind turbine this effect has been predicted, where mechanical power is the outcome of the total torque, primarily due to aerodynamic lift forces [34].

Furthermore, it is evident from the torque patterns seen at various azimuthal positions that a positive torque value on the main blade is reached prior to θ = 90˚ for both wind speeds at λ = 0.5 and λ = 0.9 (Figure 4.8). However, beyond this point, the torque is negligible or even negative. Though λ = 0.9 showed 30% larger torque magnitude differences between the two wind speeds than λ = 0.5, similar torque patterns were seen at both λ.

Regarding the results obtained in this work, increases in the tip speed-ratio can result in torque pulsation reductions, which can be explained by the flow's better ability to remain attached to the blade surface. Ahmedov & Ebrahimi [61] have examined this by simulating a four-bladed H-Darrieus wind turbine in turbulent conditions. This seems to be in line with the torque results for both moderate (8 m/s) and high (20 m/s) wind speeds shown in Figure 4.8.

4.2.4 Wind speed effect on power coefficient

As previously mentioned, the torque on the three blades increases considerably, with the average C_p values remaining at similar levels at high wind speeds (Figure3.6). Similarly, the C_p changes during a complete rotor's rotation are almost the same for both wind speeds, either at λ = 0.5 or at λ = 0.9, with minimal differences in their magnitudes, as shown in Figure4.9.

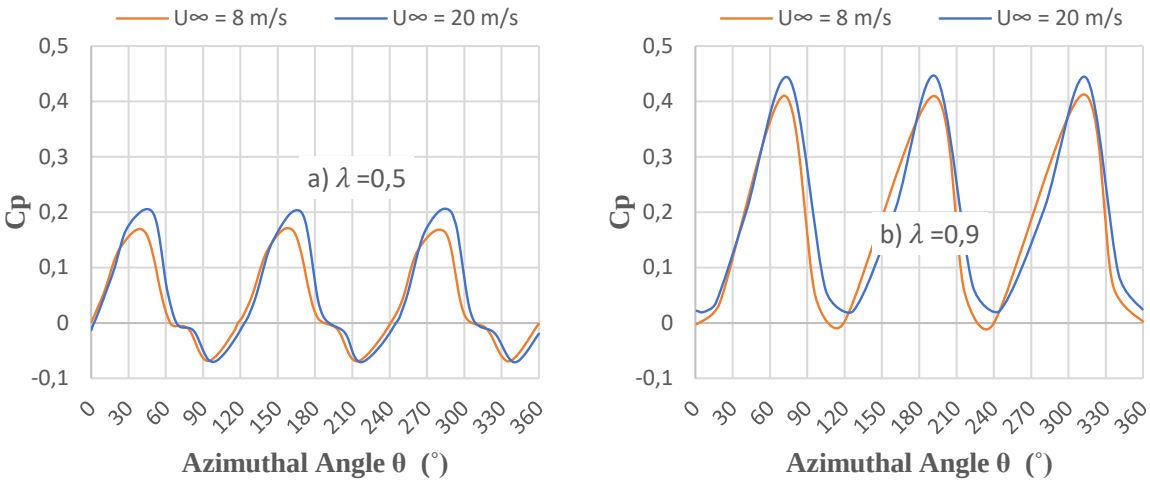

Figure 4.9 Power Coeffcient vs Azimuthal Angle, for U∞ = 8 m/s and U∞ = 20 m/s at (a) λ = 0.5 and (b) λ = 0.9, Using the Previously Presented 2D Model

According to (Equation 15), it is apparent that the maximum value of C_p is obtained at a maximum overall torque (T). This occurs at azimuthal angles (θ) that are close to those of the torque peak values for each one of the blades. In the case of the main blade, when U_∞ = 8 m/s, the azimuthal angles for the maximum C_p were θ = 48˚ and θ = 74˚ at λ = 0.5 as at λ = 0.9. Torque peak values were obtained at θ = 46˚ and θ = 72˚, respectively. Similar behavior was observed for U_∞= 20 m/s.

4.3 Velocity and pressure contours

4.3.1 Velocity contours

Velocity contours provide essential insights into the interaction between VAWT blades and the airflow. They reveal details about boundary layer development, flow separation, and reattachment. High-velocity regions near the blades highlight areas of effective energy extraction, while low-velocity zones indicate inefficiencies.

At λ = 0.5, the turbine operates at a relatively low rotational speed compared to the wind speed. The velocity contours reveal that the wake behind the turbine is relatively weak, suggesting that the turbine is not extracting a significant amount of energy from the wind. The flow field around the blades is disturbed, with noticeable flow separation and vortex shedding, indicative of inefficiencies. High-velocity regions near the leading edge are limited, while low-velocity zones near the trailing edge dominate, showing a lack of streamlined interaction between the blades and the surrounding airflow.

At λ = 0.9, the turbine operates at a higher rotational speed relative to the wind speed. The wake behind the turbine becomes more pronounced, demonstrating improved energy extraction. The velocity contours display a smoother flow field around the blades, with reduced flow separation and vortex shedding, which are hallmarks of efficient aerodynamic performance at higher *TSR*s. High-velocity regions near the leading edge are more distinct, indicating better acceleration caused by blade rotation and wind interaction, while low-velocity zones near the trailing edge are minimized, suggesting reduced inefficiencies.

When comparing the contours at *TSR*s of 0.5 and 0.9, the differences in wake strength and flow smoothness become evident. The contours reveal periodic changes in the velocity field caused by blade rotation, with noticeable turbulent patterns and vortices downstream. These wake formations influence aerodynamic performance, affecting lift, drag, and torque generation. Despite these differences, the figures at wind speeds of 8 m/s and 20 m/s show almost identical patterns at key azimuthal angles, albeit with varying intensity of velocity values.

Analyzing these patterns inform blade design optimization, refinement of airfoil profiles, and operational adjustments to enhance energy extraction, minimize losses, and improve overall VAWT performance.

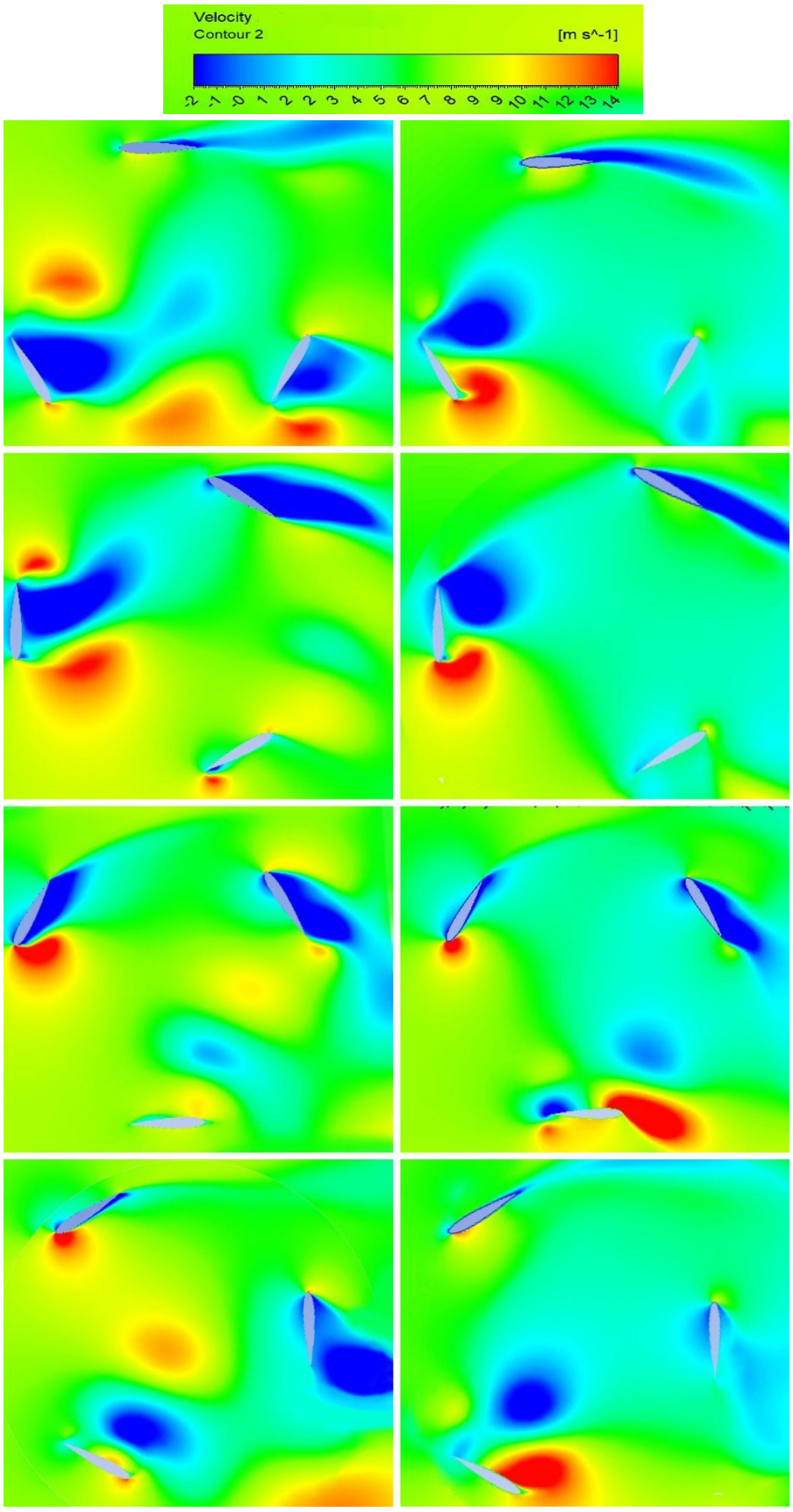

Figure 4.10 Velocity Contours Around VAWT Blades for U_∞ =8 m/s Wind Speed at λ = 0.5 (Left) and λ = 0.9 (Right) Across Key Azimuthal Angles (0°, 90°, 180°, 270°)

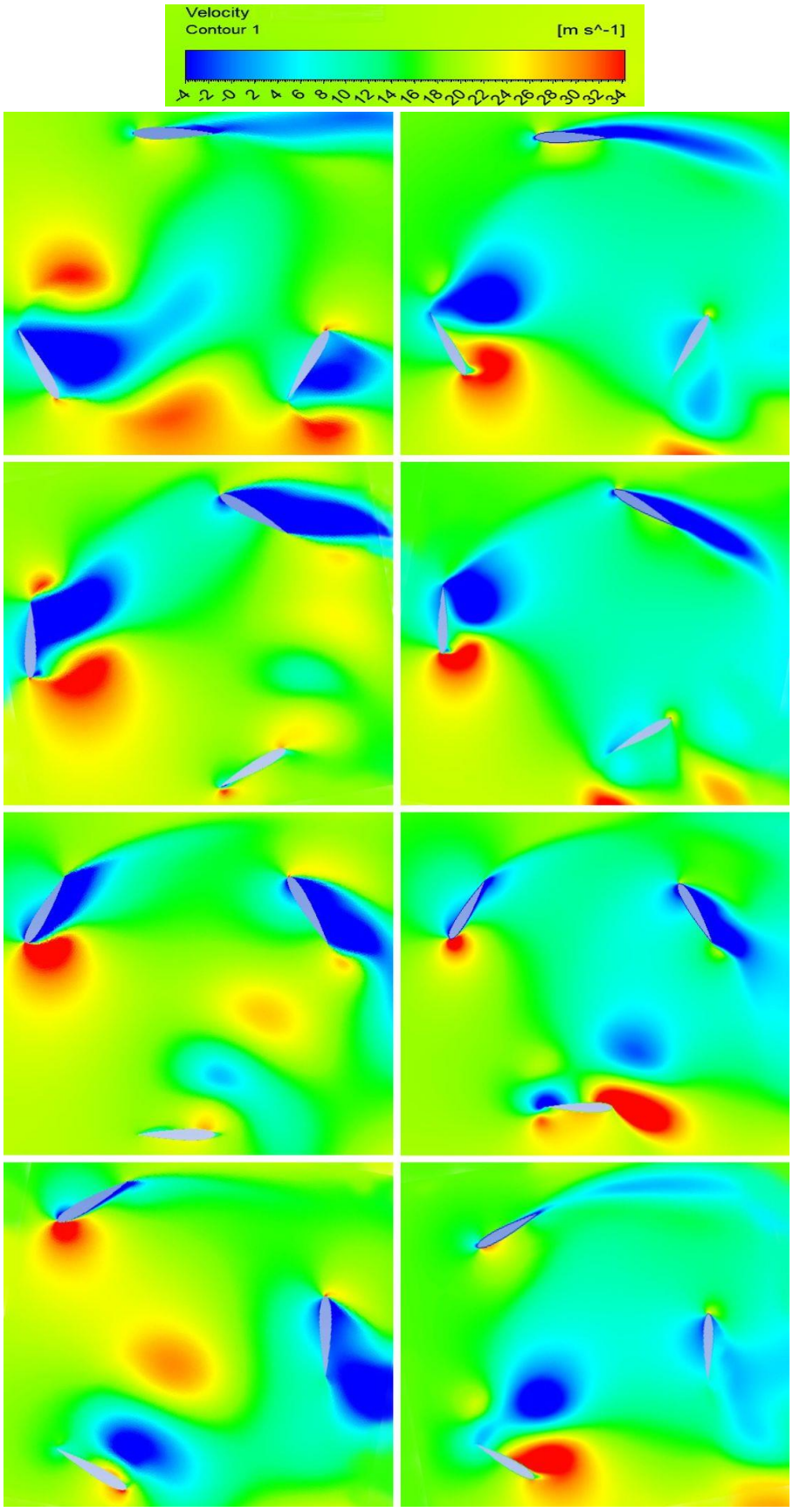

Figure 4.11 Velocity Contours Around VAWT Blades for U_∞ =20 m/s Wind Speed at λ = 0.5 (Left) and λ = 0.9 (Right) Across Key Azimuthal Angles (0°, 90°, 180°, 270°)

4.3.2 Pressure contours

The analysis of pressure contours around Vertical Axis Wind Turbine (VAWT) blades offers crucial insights into the aerodynamic forces influencing their performance. For wind speeds of 8 m/s and 20 m/s, as shown in Figures 4.12 and 4.13, these contours highlight how pressure varies across the blade surfaces, driving the lift and drag forces essential for turbine operation. High-pressure zones typically form on the windward side of the blades, while low-pressure regions appear on the leeward side, creating the pressure difference that generates lift. The cyclic blade motion causes this distribution to change periodically, influencing aerodynamic forces throughout each rotation.

At $\lambda = 0.5$, a significant low-pressure region develops on the intrados (suction side) of the blades, particularly near the leading edge, driving lift and rotation. However, the pressure on the extrados (pressure side) recovers relatively quickly after the leading edge. The wake behind the turbine at this *TSR* is relatively weak, indicating limited energy extraction from the wind. Conversely, at $\lambda = 0.9$, the low-pressure region on the intrados is more intense, signifying increased lift generation and higher power extraction. Pressure recovery on the extrados is slower, resulting in a larger low-pressure area, a more pronounced wake, and significant energy extraction. However, at higher angles of attack, flow separation on the intrados may occur, potentially reducing efficiency.

Key flow behaviors, such as stagnation points and adverse pressure gradients, are evident in these pressure contours. Adverse gradients may lead to flow separation, increasing drag and reducing efficiency. These patterns underscore the influence of blade geometry, *AoA*, and airfoil profile on the pressure distribution and overall aerodynamic performance.

When comparing Figures 4.12 and 4.13, similar trends are observed in the same regions, with pressure magnitudes several times higher both positively and negatively. This highlights the scaling effects of wind speed on aerodynamic loads and energy extraction. Such analyses are beneficial in understanding the aerodynamic loads acting on the blades, which is crucial for improving efficiency and maintaining structural reliability. Pressure contour analysis helps guide design modifications, such as optimizing the airfoil shape or adjusting blade angles, to enhance performance and reduce energy losses. This makes it an essential tool for refining VAWT designs.

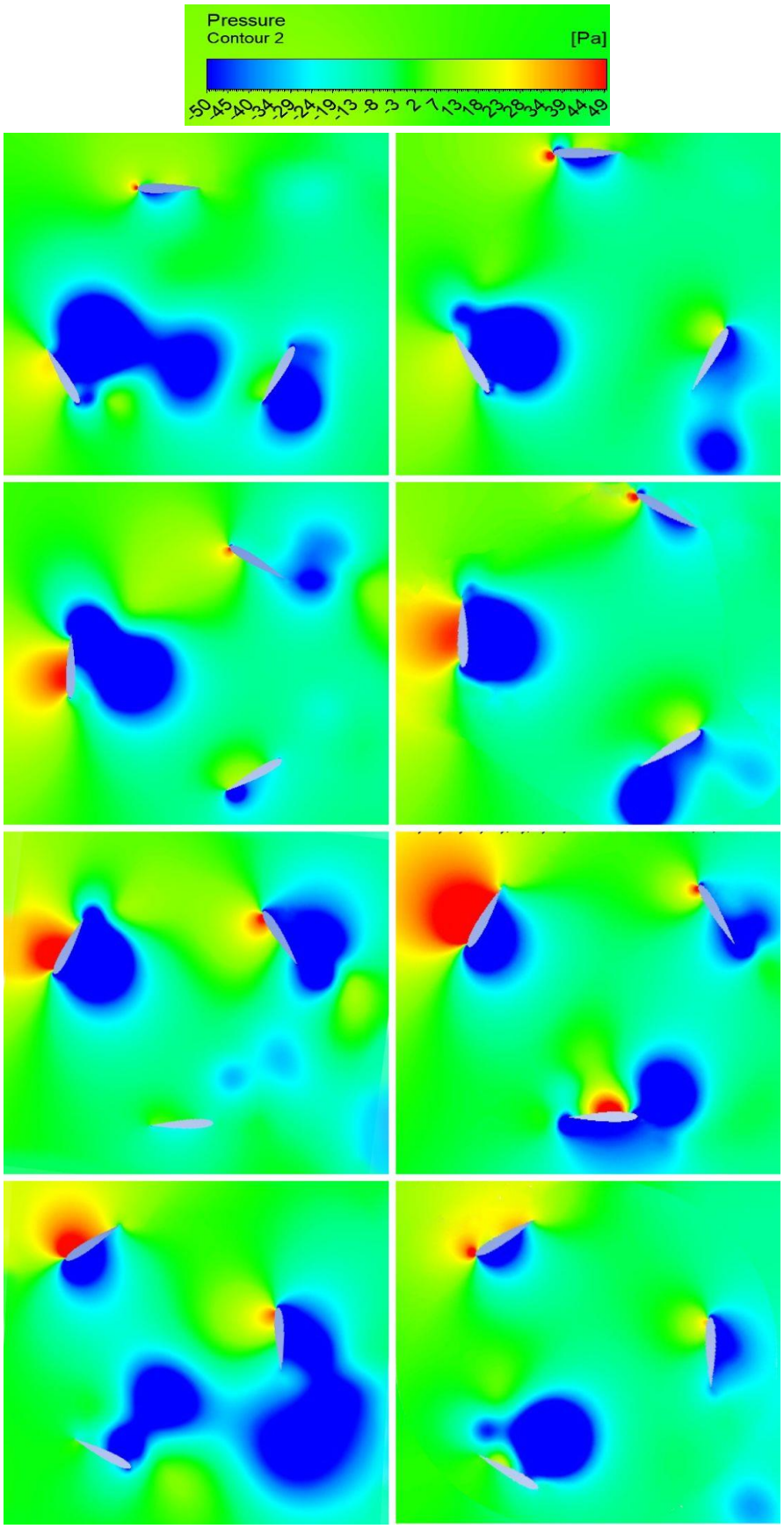

Figure 4.12 Pressure Contours Around VAWT Blades for U_∞ =8 m/s Wind Speed at λ = 0.5 (Left) and λ = 0.9 (Right) Across Key Azimuthal Angles (0°, 90°, 180°, 270°)

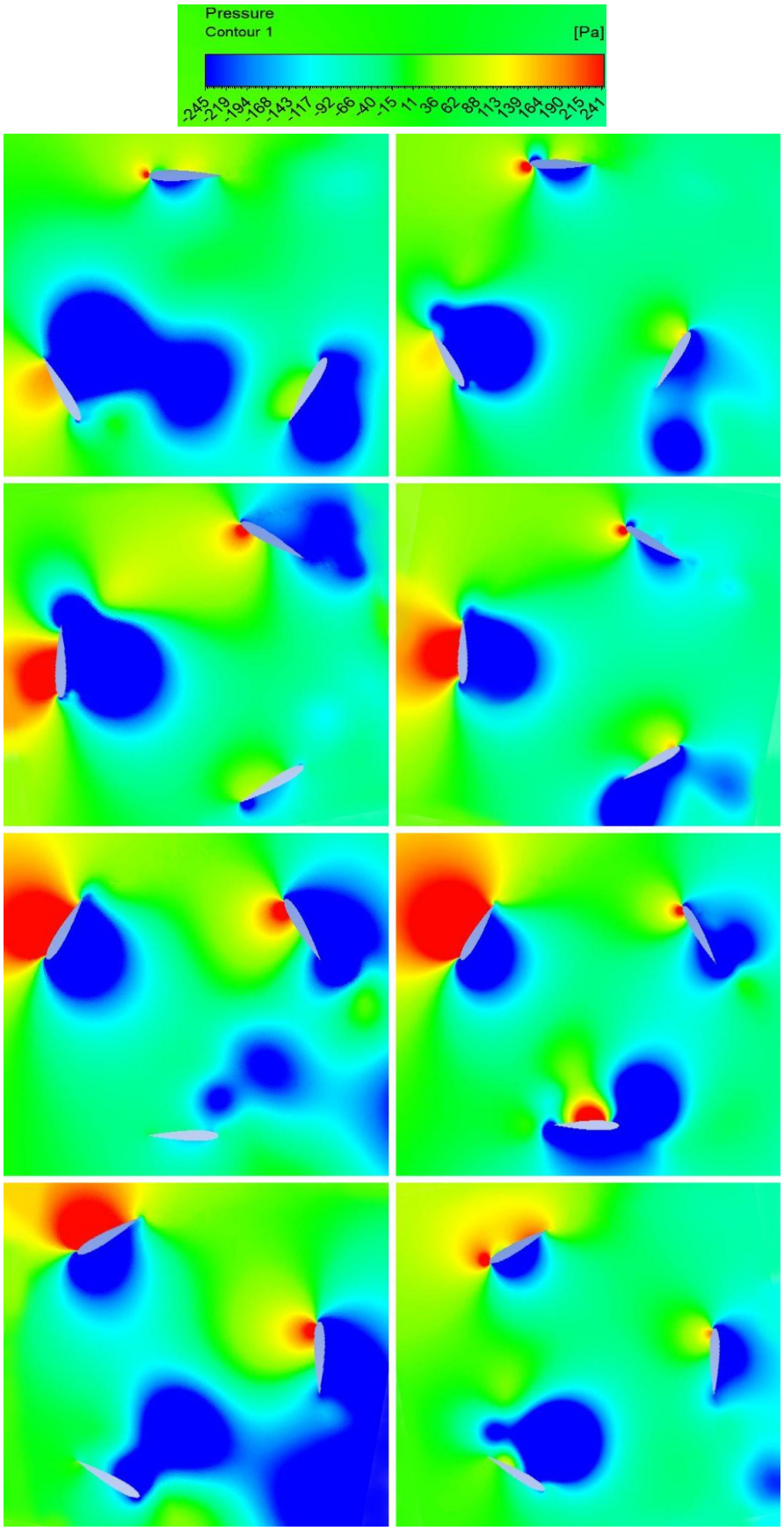

Figure 4.13 Pressure Contours Around VAWT Blades for U_∞ =20 m/s Wind Speed at λ = 0.5 (Left) and λ = 0.9 (Right) Across Key Azimuthal Angles (0°, 90°, 180°, 270°)

4.4 Conclusion

This chapter provided a comprehensive discussion of the performed CFD analysis, the results highlighted the influence of wind speed and *TSR* on key performance parameters such as torque, lift and drag forces, and power coefficient. Maximum drag forces were observed at azimuthal angles of 65°–85°, while peak torque occurred at 45°–50° (31.1°–33.8°) for λ = 0.5 and 72°–78° (38.2°–41.4°) for λ = 0.9, with higher torque recorded at 20 m/s compared to 8 m/s. However, turbulence and vorticity at higher wind speeds caused slight reductions in rotor efficiency, particularly beyond 90° azimuthal angles, where flow separation and vorticity significantly reduced torque output.

The velocity and pressure contours analysis further demonstrate the flow behavior around the blades. At λ = 0.5, the turbine exhibited weak wake structures, noticeable flow separation, and lower aerodynamic efficiency, whereas at λ = 0.9, the wake was more developed, with smoother flow patterns, reduced separation, and enhanced energy extraction. Pressure contour evaluations revealed periodic high and low-pressure zones that drive lift and drag forces, emphasizing the role of blade geometry and motion in aerodynamic performance. These findings underscore the cyclic nature of aerodynamic forces and their impact on the turbine's rotational dynamics.

CHAPTER 5:

Conclusions and Future work

5.1 General conclusion

On the regard of this thesis, the study conducted a comprehensive investigation into the performance of a high-solidity VAWT under moderate to high wind conditions, utilizing a 2D CFD approach based on the SST k-ω turbulence model. By developing and solving the unsteady Reynolds-averaged Navier-Stokes (URANS) equations, detailed insights were provided into the aerodynamic behavior of the turbine, including the influence of *TSR* and wind speeds on torque, lift, drag forces, and overall efficiency.

The results highlighted the turbine's performance across varying operational conditions. At moderate wind speeds and lower *TSR*s, the turbine experienced significant flow separation and weaker wake structures, which limited aerodynamic efficiency. Conversely, at higher *TSR*s and wind speeds, the flow around the blades became more organized, resulting in smoother wakes, reduced separation, and improved energy extraction. Critical azimuthal angles were identified for peak torque and drag forces, emphasizing the importance of blade positioning and aerodynamic optimization in turbine performance.

While higher wind speeds increased power output and torque, they also introduced greater turbulence and vorticity, leading to slight reductions in rotor efficiency at certain azimuthal angles, particularly beyond 90°, where flow separation was most pronounced. The study's velocity and pressure contour analyses further illustrated the dynamic interplay of high and low-pressure zones driving lift and drag forces, underscoring the cyclic nature of aerodynamic loading.

The application of CFD, combined with the SST k-ω model, proved effective in capturing the complex unsteady phenomena governing VAWT performance. This methodology balanced computational cost with the need for accurate simulation of turbulent flows, providing a robust foundation for analyzing and optimizing turbine behavior.

This thesis has significantly contributed to understanding the aerodynamic performance of high-solidity VAWTs operating under moderate to high wind conditions, offering valuable insights into their dynamic behavior and operational efficiency.

5.2 Future work

Several areas of future research are suggested in order to fatherly enhance the analysis and design of the high-solidity VAWT. A parametric study should be performed to assess how various design parameters, including blade length, number of blades, solidity, and rotor shape, affect the turbine's performance. This will allow for the identification of optimal configurations under different wind conditions and *TSR*s.

In addition, applying optimization methods such as Genetic Algorithms or Gradient-Based Optimization can help refine the blade geometry and operational settings to achieve maximum power output and energy efficiency. Which may help balancing between lift and drag forces for an improved performance.

Exploring the integration of a variable pitch mechanism would also be beneficial. Such a system would enable dynamic adjustment of the blade's *AoA*, allowing the turbine to adapt to varying wind speeds and thereby enhance torque and power generation across a wider range of operational conditions.

Another important step is to incorporate 6 Degrees of Freedom (6DoF) simulations within Fluent to account for the inertia and dynamic behavior of the turbine components. These simulations would provide a more realistic and accurate representation of the rotor's motion, including gyroscopic effects and rotational dynamics.

Finally, Fluid-Structure Interaction (FSI) simulations should be considered to study the interaction between the aerodynamic forces and the turbine blades. This would help to predict how blade deformation affects performance and improve the overall understanding of the turbine's durability and efficiency under different load conditions.

5.2.1 Future work summary

- Evaluate the effects of design parameters like blade geometry, N, and σ.
- Use optimization methods to refine blade design based on operating conditions.
- Investigate dynamic blade angle adjustment for varying wind speeds.
- Implement simulations to model dynamic component behavior and inertia effects.
- Study how blade deformation impacts performance and turbine longevity.

Bibliograpy

[1] IEA, "Key World Energy Statistics," IEA Publishing, Paris, 2021.

[2] Ministry. of. Energy. Algeria, "Electricity and Gas," 2017. Accessed: 2024/02/24 02:49:38. [Online]. Available: https://www.energy.gov.dz/?rubrique=electricite-et-gaz#527

[3] D. Djemati, "Étude de l'écoulement autour d'une éolienne de type Savonius et simulation des performances de l'éolienne," Mémoire de magistère en physique, Université de Batna, 2011.

[4] Global. Wind. Eenergy. Council, "Global Wind Report - Annual Market Update," 2024.

[5] F. Chellali, A. Khellaf, A. Belouchrani, and A. Recioui, "A contribution in the actualization of wind map of Algeria," *Renewable and Sustainable Energy Reviews*, vol. 15, no. 2, pp. 993-1002, 2011.

[6] W. W. E. Association, "Small Wind World Report," Bonn, Germany, 2017.

[7] F. König, *Windenergie in praktischer Nutzung*. Pfriemer, 1976.

[8] W. F. d. Fröde Edelgard, *Windmühlen in Deutschland, Holland, Belgien : Energiespender und ästhetische Architektur* (Studio DuMont). Köln: DuMont (in German), 1981.

[9] J. C. Notebaart, *Windmühlen* (Der Stand der Forschung über das Vorkommen und den Ursprung). De Gruyter Mouton, 1972.

[10] I. M. d. l. Plaza. https://www.bbvaopenmind.com/en/technology/innovation/history-of-windpower-from-origins-to-world-war-ii/ (accessed 2024/02/30 20:49:38).

[11] T. J. Price, "James Blyth − Britain's First Modern Wind Power Pioneer," *Wind Engineering*, vol. 29, no. 3, pp. 191-200, 2005/05/01 2005, doi: 10.1260/030952405774354921.

[12] "Storing wind power ‐ Poul la cour Museet," ed.

[13] "Exploring the History and Development of Darrieus Wind Turbines - Powering Solution," ed, 2023.

[14] S. S.j, "The S-turbine and its application," *Mechanical Eng. J*, vol. 53, no. 5, pp. 333‐338, 1931 1931.

[15] "Descubrimiento de las Fuentes Energeticas timeline," in *Timetoast Timelines*, ed, 1767.

[16] "V236-15.0 MW." https://www.vestas.com/en/energy-solutions/offshore-wind-turbines/V236-15MW (accessed 2024/03/02 00:29:11).

[17] "Vestas 15 MW Turbines Selected for 495 MW Floating Wind Farm in South Korea - World-Energy." https://www.world-energy.org/article/30806.html (accessed 2024/03/02 00:41:58).

[18] M. A. Miller, S. Duvvuri, and M. Hultmark, "Solidity effects on the performance of vertical-axis wind turbines," *Flow*, vol. 1, p. E9, 2021, Art no. E9, doi: 10.1017/flo.2021.9.

[19] M. Hansen, *Aerodynamics of wind turbines*. Routledge, 2015.

[20] K. H. Bergey, "The Lanchester-Betz limit (energy conversion efficiency factor for windmills)," *Journal of Energy*, vol. 3, no. 6, pp. 382-384, 1979.

[21] P. Frédéric, "ETUDE ET COMMANDE DE GENERATRICES ASYNCHRONES POUR L'UTILISATION DE L'ENERGIE EOLIENNE - Machine asynchrone à cage autonome - Machine asynchrone à double alimentation reliée au réseau," Université de Nantes, 2003. [Online]. Available: https://theses.hal.science/tel-00011383

[22] R. H. Erich Hau, *Wind turbines: fundamentals, technologies, application, economics*. Springer, 2006.

[23] M. Islam, D. S. Ting, and A. Fartaj, "Design of a special-purpose airfoil for smaller-capacity straight-bladed VAWT," *Wind Engineering*, vol. 31, no. 6, pp. 401-424, 2007.

[24] K. Rogowski, G. Królak, and G. Bangga, "Numerical study on the aerodynamic characteristics of the NACA 0018 airfoil at low Reynolds number for Darrieus wind turbines using the transition SST model," *Processes*, vol. 9, no. 3, p. 477, 2021.

[25] I. Paraschivoiu, *Wind turbine design: with emphasis on Darrieus concept*. Presses inter Polytechnique, 2002.

[26] C. E. Soraghan, "Aerodynamic modelling and control of vertical axis wind turbines," 2014.

[27] Q. Taverne, "Modélisation par forces surfaciques d'éoliennes à axe vertical," *UCL, Université catholique de Louvain*, 2015.

[28] X. Jin, G. Zhao, K. Gao, and W. Ju, "Darrieus vertical axis wind turbine: Basic research methods," *Renewable and Sustainable Energy Reviews*, vol. 42, pp. 212-225, 2015.

[29] Y. Bazilevs, M. C. Hsu, J. Kiendl, R. Wüchner, and K. U. Bletzinger, "3D simulation of wind turbine rotors at full scale. Part II: Fluid‐structure interaction modeling with composite blades," *International Journal for numerical methods in fluids*, vol. 65, no. 1‐3, pp. 236-253, 2011.

[30] K. McLaren, S. Tullis, and S. Ziada, "Computational fluid dynamics simulation of the aerodynamics of a high solidity, small‐scale vertical axis wind turbine," *Wind Energy*, vol. 15, no. 3, pp. 349-361, 2012.

[31] S. B. Qamar and I. Janajreh, "A comprehensive analysis of solidity for cambered darrieus VAWTs," *International Journal of Hydrogen Energy*, vol. 42, no. 30, pp. 19420-19431, 2017.

[32] S. McTavish, D. Feszty, and T. Sankar, "Steady and rotating computational fluid dynamics simulations of a novel vertical axis wind turbine for small-scale power generation," *Renewable energy*, vol. 41, pp. 171-179, 2012.

[33] S. Brusca, R. Lanzafame, and M. Messina, "Design of a vertical-axis wind turbine: how the aspect ratio affects the turbine's performance," *International Journal of Energy and Environmental Engineering*, vol. 5, pp. 333-340, 2014.

[34] F. Balduzzi, A. Bianchini, R. Maleci, G. Ferrara, and L. Ferrari, "Critical issues in the CFD simulation of Darrieus wind turbines," *Renewable Energy*, vol. 85, pp. 419-435, 2016.

[35] P. Delafin, T. Nishino, L. Wang, A. Kolios, and T. Bird, "Comparison of RANS CFD and lower-order aerodynamic models for 3D Vertical Axis Wind Turbines," *EWEA*, 2015.

[36] P. Chatterjee and R. N. Laoulache, "Performance modeling of ducted vertical axis turbine using computational fluid dynamics," *Marine Technology Society Journal*, vol. 47, no. 4, pp. 36-44, 2013.

[37] M. Mohamed, "Performance investigation of H-rotor Darrieus turbine with new airfoil shapes," *Energy*, vol. 47, no. 1, pp. 522-530, 2012.

[38] H. Beri and Y. Y. Yao YingXue, "Effect of camber airfoil on self starting of Vertical Axis Wind Turbine," 2011.

[39] T. Maître, E. Amet, and C. Pellone, "Modeling of the flow in a Darrieus water turbine: Wall grid refinement analysis and comparison with experiments," *Renewable energy*, vol. 51, pp. 497-512, 2013.

[40] S. Lain and C. Osorio, "Simulation and evaluation of a straight-bladed Darrieus-type cross flow marine turbine," 2010.

[41] F. Trivellato and M. R. Castelli, "On the Courant‐Friedrichs‐Lewy criterion of rotating grids in 2D vertical-axis wind turbine analysis," *Renewable energy*, vol. 62, pp. 53-62, 2014.

[42] C. S. Ferreira, H. Bijl, G. van Bussel, and G. Van Kuik, "Simulating dynamic stall in a 2D VAWT: modeling strategy, verification and validation with particle image velocimetry data," in *Journal of physics: conference series*, 2007, vol. 75, no. 1: IOP Publishing, p. 012023.

[43] A. Untaroiu, H. G. Wood, P. E. Allaire, and R. J. Ribando, "Investigation of self-starting capability of vertical axis wind turbines using a computational fluid dynamics approach," 2011.

[44] B. Yang and C. Lawn, "Fluid dynamic performance of a vertical axis turbine for tidal currents," *Renewable Energy*, vol. 36, no. 12, pp. 3355-3366, 2011.

[45] M. R. Castelli, A. Englaro, and E. Benini, "The Darrieus wind turbine: Proposal for a new performance prediction model based on CFD," *Energy*, vol. 36, no. 8, pp. 4919-4934, 2011.

[46] M. Raciti Castelli, G. Ardizzon, L. Battisti, E. Benini, and G. Pavesi, "Modeling strategy and numerical validation for a Darrieus vertical axis micro-wind turbine," in *ASME International Mechanical Engineering Congress and Exposition*, 2010, vol. 44441, pp. 409-418.

[47] R. Howell, N. Qin, J. Edwards, and N. Durrani, "Wind tunnel and numerical study of a small vertical axis wind turbine," *Renewable energy*, vol. 35, no. 2, pp. 412-422, 2010.

[48] A. Rossetti and G. Pavesi, "Comparison of different numerical approaches to the study of the H-Darrieus turbines start-up," *Renewable energy*, vol. 50, pp. 7-19, 2013.

[49] J. McNaughton, F. Billard, and A. Revell, "Turbulence modelling of low Reynolds number flow effects around a vertical axis turbine at a range of tip-speed ratios," *Journal of Fluids and Structures*, vol. 47, pp. 124-138, 2014.

[50] R. Lanzafame, S. Mauro, and M. Messina, "2D CFD modeling of H-Darrieus wind turbines using a transition turbulence model," *Energy Procedia,* vol. 45, pp. 131-140, 2014.

[51] F. R. Menter, "Two-equation eddy-viscosity turbulence models for engineering applications," *AIAA journal,* vol. 32, no. 8, pp. 1598-1605, 1994.

[52] F. R. Menter, M. Kuntz, and R. Langtry, "Ten years of industrial experience with the SST turbulence model," *Turbulence, heat and mass transfer,* vol. 4, no. 1, pp. 625-632, 2003.

[53] A. Fluent, "Ansys fluent theory guide," *Ansys Inc., USA,* vol. 15317, pp. 724-746, 2011.

[54] M. Elkhoury, T. Kiwata, and E. Aoun, "Experimental and numerical investigation of a three-dimensional vertical-axis wind turbine with variable-pitch," *Journal of wind engineering and Industrial aerodynamics,* vol. 139, pp. 111-123, 2015.

[55] J. He *et al.*, "CFD modeling of varying complexity for aerodynamic analysis of H-vertical axis wind turbines," *Renewable Energy,* vol. 145, pp. 2658-2670, 2020.

[56] H. Lam and H. Peng, "Study of wake characteristics of a vertical axis wind turbine by two-and three-dimensional computational fluid dynamics simulations," *Renewable Energy,* vol. 90, pp. 386-398, 2016.

[57] N. Ma *et al.*, "Airfoil optimization to improve power performance of a high-solidity vertical axis wind turbine at a moderate tip speed ratio," *Energy,* vol. 150, pp. 236-252, 2018.

[58] A. Rezaeiha, H. Montazeri, and B. Blocken, "On the accuracy of turbulence models for CFD simulations of vertical axis wind turbines," *Energy,* vol. 180, pp. 838-857, 2019.

[59] A. Orlandi, M. Collu, S. Zanforlin, and A. Shires, "3D URANS analysis of a vertical axis wind turbine in skewed flows," *Journal of Wind Engineering and Industrial Aerodynamics,* vol. 147, pp. 77-84, 2015.

[60] C. Song, G. Wu, W. Zhu, X. Zhang, and J. Zhao, "Numerical investigation on the effects of airfoil leading edge radius on the aerodynamic performance of H-rotor Darrieus vertical axis wind turbine," *Energies,* vol. 12, no. 19, p. 3794, 2019.

[61] A. Ahmedov and K. Ebrahimi, "Numerical Modelling of an H-type Darrieus Wind Turbine Performance under Turbulent Wind," *American Journal of Energy Research,* vol. 5, no. 3, pp. 63-78, 2017.

Appendix:
NACA 0018 airfoil co-ordinates

Table NACA 0018 Airfoil Coordinates

X	Y
1	0,00189
0,95	0,0121
0,9	0,02172
0,8	0,03935
0,7	0,05496
0,6	0,06845
0,5	0,07941
0,4	0,08705
0,3	0,09003
0,25	0,08912
0,2	0,08606
0,15	0,08018
0,1	0,07024
0,075	0,063
0,05	0,05332
0,025	0,03922
0,0125	0,02841
0	0
0,0125	-0,02841
0,025	-0,03922
0,05	-0,05332
0,075	-0,063
0,1	-0,07024
0,15	-0,08018
0,2	-0,08606
0,25	-0,08912
0,3	-0,09003
0,4	-0,08705
0,5	-0,07941
0,6	-0,06845
0,7	-0,05496
0,8	-0,03935
0,9	-0,02172
0,95	-0,0121
1	-0,00189